

Effect of *o*-difluoro and *p*-methyl substituents on the structure, optical properties and anti-inflammatory activity of phenoxy thiazole acetamide derivatives: Theoretical and experimental studies

Hussien Ahmed Khamees^a, Yasser Hussein Eissa Mohammed^{b, c}, Ananda S^a, Fares Hezam Al-Ostoot^{b, d}, Sangappa Y^e, Saad Alghamdi^f, Shaukath Ara Khanum^b, Mahendra Madegowda^{a, *}

^a Department of Studies in Physics, Manasagangotri, University of Mysore, Mysuru, 570006, Karnataka, India

^b Department of Chemistry, Yuvaraja's College, University of Mysore, Mysuru, 570005, Karnataka, India

^c Department of Biochemistry, Faculty of Applied Science College, University of Hajjah, Yemen

^d Department of Biochemistry, Faculty of Education & Science, University of Albaydaa, Yemen

^e Department of Physics, Mangalore University, Mangalore, Karnataka State, 574199, India

^f Laboratory Medicine Department, Faculty of Applied Medical Science, Umm Al-Qura University, Makkah, Saudi Arabia

ARTICLE INFO

Article history:

Received 11 July 2019

Received in revised form

26 August 2019

Accepted 2 September 2019

Available online 6 September 2019

Keywords:

DFT studies

Energy framework

In silico docking

In vitro COX

Molecular dynamics

Structural analysis

ABSTRACT

Thiazole derivatives (**6a** and **6b**) have been synthesized and characterised by ¹H – ¹³C NMR, as well as LC-MS spectra. The three-dimensional structures have been confirmed by single crystal X-ray diffraction method. **6a** and **6b** compounds have been crystallized in the Triclinic and the Orthorhombic systems with *P*-1 and *Pbca* space groups, respectively. Supramolecular structures revealed the stability of molecules with different intermolecular interactions and different crystal packing environment. Theoretical study by Density functional theory (DFT) with B3LYP functional based on highest basis set 6-311++G(d,p) was employed to calculate the geometry and compared to the experimental data. The electronic structures and intramolecular charge transfers have been investigated by using natural population and natural bond orbital analysis (NBO). Further, DFT studies were performed to assess the frontier molecular orbitals (FMOs), energy gap, softness, hardness, and others chemical reactivity. Hirshfeld surface was investigated to distinguish the different interatomic contacts and understand the crystal packing of molecules with aid of energy frameworks through different intermolecular interaction energies based on the anisotropy of the topology. Nonlinear optical property (NLO) of the synthesized molecules were predicted by (DFT) and examined experimentally by using second harmonic generation (SHG) and revealed the importance of high NLO based on the nature of substituents and conformation. Thiazole derivatives were assessed for anti-inflammation activity by *in silico* molecular docking studies against COX-1 and COX-2 protein receptors revealed prominent interactions with active site and further molecular dynamics confirms the stability of the protein-ligand model. *In vitro* assay against cyclooxygenase (COX) enzyme gave IC₅₀ values of **6a** and **6b** molecules with *ortho*-difluoro and *para*-methyl positions on benzoyl group, showed better inhibitor for COX-1 and COX-2, respectively.

© 2019 Elsevier B.V. All rights reserved.

1. Introduction

Thiazole moiety is one of the organic heterocyclic rings that comprises nitrogen and sulphur atoms. Its derivatives are the most

bioactive important compounds in pharmacological field that plays a major role in designing new pharmacologically active drugs and to develop the existed ones, which are extensively exploited in the medicinal chemistry [1] with versatile activities like: anti-oxidant [2], antipsychotic [3], antibacterial [4], antitumor [5] and anti-inflammatory [6].

The inflammation is well known multifactorial process that specifically defines as local responses of mammalian tissues to the injury by any agent. In more details, it is a multiple sequence of a

* Corresponding author. DOS in Physics, Manasagangotri, University of Mysore, Mysuru, 570006, Karnataka, India.

E-mail address: mahendra@physics.uni-mysore.ac.in (M. Madegowda).

cellular and molecular responses acquired throughout the evolution to eliminate external agents and then give promotion to repair the damaged tissues. Fundamentally, the inflammation can be categorized into two types: acute and chronic. Acute inflammation type is a fast response to the injurious agent. On the onset of such injury there could be promulgation to deliver mediators of host defense-leukocytes and plasma proteins at the injury site. On the other hand, the chronic inflammation response has prolonged inflammation duration (weeks to months to years). This could proceed with active inflammation and injury simultaneously [7,8].

Among all strategies and methods available for treatment of inflammation, the two groups of arachidonic acid metabolites: prostaglandins and leukotrienes produced by Cyclooxygenase (COX) and Lipoxygenase (LOX) respectively, play significant role in inflammation, where the free steroidal anti-inflammatory drugs usually inhibit the COX-1 isoenzyme or the combination isoenzymes of COX-1 and COX-2 [8].

Since more than two decades, the researchers and pharmacists have focused on the synthesis and development of the thiazole derivatives as anti-inflammatory agents. Pawan K. Sharma et al. (1997) [9] prepared a series of 1,2-benzisothiazole compounds with thiazolyl-acetic acid moiety and evaluated the anti-inflammation activity; the molecule with *para*-chlorophenyl substituents registered as the most potent anti-inflammatory molecule.

B. Shivarama Holla et al. (2003) [10] synthesized and screened the anti-inflammatory and antibacterial properties of a series of 2,4-disubstituted thiazole. The authors have reported the compounds with 3-Cl, 4-F phenyl and 4-Cl substituents are the best potent anti-inflammatory activity having 94% and 93% of oedema inhibition in comparison to that of standard ibuprofen. Also, Pran Kishore Deb et al. (2013) [11] have reported on the synthesis and anti-inflammatory activity of some benzothiazole acetamide derivatives and suggested that the compounds with chloro and fluorophenyl substituents exhibited good anti-inflammatory activities with 95% and 88% of the standard indomethacin. Other researchers also revealed the significance of amino group at the para position of the thiazole ring, which has an increase in anti-inflammatory activity [12].

In addition, thiazole derivatives have been proved the enhancement of nonlinear optical property (NLO), exceptionally with unsymmetrical thiazole rings and lengthy π -conjugated

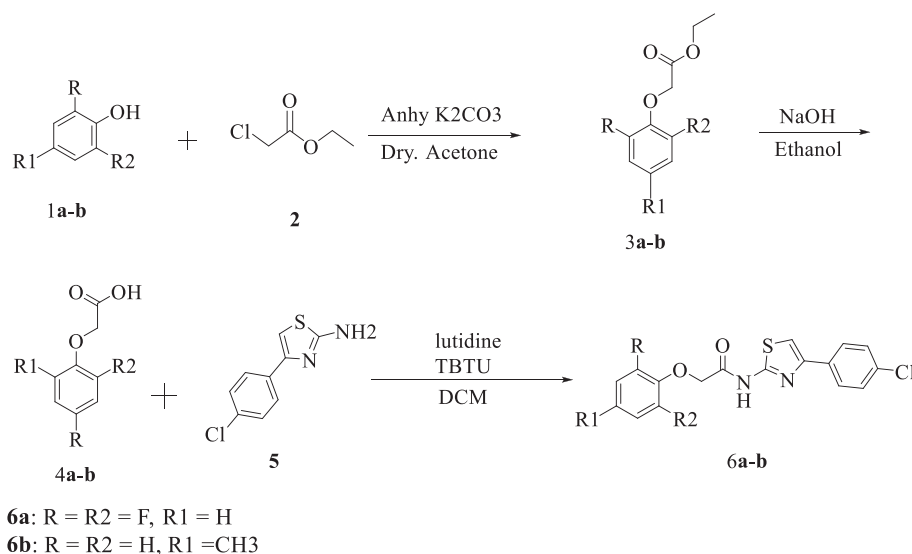
system, which typically possess a worth value of second harmonic generation (SHG) [13,14], which is suitable for technological and industrial applications of electronic and optical materials. The importance of thiazole ring as NLO materials has been studied and confirmed widely in various experimental [15] and theoretical [13] methods. Such property has been impacted by mutual affecting factors which includes asymmetric polarization, conjugate length, degree of linearity conformation, intramolecular charge transfer (ICT), types of donor and acceptor groups as well as their position [16–18]. The registered patents of thiazole derivatives are a proof of their importance in both industrial and pharmaceutical fields [19].

In view of the above facts and information observed from the literature, it is clear to reveal that the combination of thiazole moiety with 4-chloro phenyl, acetamide and fluorine substituents are important for the profound anti-inflammatory activity. Hence, motivated by the above literature, we have made pertinent objectives to synthesize 2-(phenoxy)-N-(4-(4-chlorophenyl) thiazol-2-yl) acetamide (Scheme 1), which specifically target to study the effect of para methyl and 2,6 ortho fluorine substituents on the phenoxy ring of the thiazole derivative; including structural characterization, supramolecular, electron population, HOMO-LUMO, electrostatic and molecular electrostatic potential (ESP-MEP), nonlinear optical property (NLO), Hirshfeld surface analysis and energy frameworks as well as anti-inflammatory activities of the compounds. In addition, these compounds were tested theoretically to know the fitness and binding possessions of the compounds in the active site of COX-1 (pdb ID:1eqg) and COX-2 (pdb ID:1pxx) receptors by using docking and molecular dynamic simulation methods.

2. Procedures and instruments

2.1. Materials and methods

All chemicals have been bought from the Sigma Aldrich Chemical Co. Thin layer chromatographic technique were used to check the purity of the compounds under UV-lamp with $\lambda = 254$ nm. Boiling and melting points have been recorded with a digital thermometer on the Chemiline, Microcontroller based melting point/boiling point-CI725 apparatus. ^1H and ^{13}C NMR spectra have been determined on VNMRS-400 "Agilent-NMR" with using



Scheme 1. Synthesis of 2-(phenoxy)-N-(4-(4-chlorophenyl) thiazol-2-yl) acetamide derivatives.

dimethyl sulphoxide solvent. Chemical shifts recorded in parts/million downfield of tetramethylsilane. The ElementarVario EL III elemental analyzer has been used for elemental analysis (N, C, and H), where the result exhibited within $\pm 0.4\%$ of the theoretical values. Mass spectra has been recorded on VG70-70H spectrophotometer.

2.2. Synthesis

Synthesis of 2-(phenoxy)-N-(4-(4-chlorophenyl) thiazol-2-yl) acetamide derivatives were implemented as shown in Scheme 1. Initially with the dry acetone as the solvent obtained ethyl 2-phenoxyacetate, which has been hydrolyzed with the solution of sodium hydroxide to provide 2-phenoxyacetic acid, the esterification of phenols with ethylchloroacetate are done with anhydrous potassium carbonate. The final compounds were synthesized by joining 2-phenoxyacetic acid with 4-(4-chlorophenyl) thiazol-2-amine by using dichloromethane as a solvent and 2,6-lutidine as a base as well as *o*-(benzotriazol-1-yl)-*N,N,N',N'*-tetra methyl uranium tetra fluoro borate as coupling agent. The reaction was monitored by thin layer chromatography. The spectral data for the final compounds **6a** and **6b** are presented in the Supplementary Material (Fig. S1-S8).

2.3. X-ray intensity data collection strategy

The X-ray intensity data for both **6a** and **6b** molecules were recorded at temperature of 293(2) K on a Bruker AXS kappa Apex2 CCD Diffractometer, with fine-focus sealed tube radiation source and 0.71073 Å wavelength of MoK α radiation. The procedure and reduction of data set was accomplished completely by using *SAINTE PLUS* [20]. *SHELXS* and *SHELXL* programs [21] have been adopted to solve and refine the structure, respectively. While the geometrical calculations, molecular figures and Crystal packing were generated and visualized by *PLATON* and *MERCURY* software, respectively [22,23]. CCDC numbers: 1842848 and 1828753 contains full crystallographic data of **6a** and **6b** crystals respectively, and available online at Cambridge crystallographic data centre.

2.4. Nonlinear optical property (NLO)

The experiment of NLO property was performed at the Indian Institute of Science (IISc), Bengaluru, according to the method of classical powder that developed by Kurtz and Perry [24] to investigate SHG efficiency. In this method, the samples were powdered in microcrystalline state and then tightly filled in a capillary glass tube. These were exposed to Nd:YAG laser with a wavelength of 1064 nm, 1.2 mJ input energy and 10 Hz repetition frequency. The references materials were Urea and KDP samples with of 60 mV and 17 mV output values, respectively.

2.5. In vitro COX assay

By using an enzyme immunoassay (EIA) kit (catalog number 560101, Cayman Chemical, Ann Arbor, MI, USA), the procedures have been described in the Supplementary Material (subsection 1.2).

2.6. Computational studies

2.6.1. Density functional theory calculation (DFT)

The most suitable function for organic compounds "B3LYP" (Becke's three parameter (B3)) [25] has been adopted in DFT model for whole theoretical calculations, by using Gaussian09 and

Gaussview5.0 programs under 6-311++G(d,p) bases set [26].

2.6.2. Hirshfeld surface analysis and energy framework calculations

The intermolecular contacts, 2D fingerprint and energy framework of the title compounds have been studied by using Crysta-Explorer17.5 program [27]. The molecular Hirshfeld surface is one of the best graphical visualization for realising the intermolecular interactions in 3D simulation. Such surface is built on d_{norm} given by equation (1).

$$d_{\text{norm}} = \left(d_i - r_i^{\text{vdw}} / r_i^{\text{vdw}} \right) + \left(d_e - r_e^{\text{vdw}} / r_e^{\text{vdw}} \right) \quad (1)$$

where d_i and d_e are the distances from the surface to the nearest inside and outside atoms, respectively, and r_i^{vdw} and r_e^{vdw} are the van der Waals radii of the contact.

Energy frameworks are considered as a powerful method to understand the crystal packing of molecules by combining the different intermolecular interaction energies including electric (E_{ele}), dispersion (E_{dis}), polarization (E_{pol}), repulsion (E_{rep}) and total (E_{tot}) energy based on the anisotropy of the topology of pairwise intermolecular interaction energies. The cylinders are representation of interaction energies between the two molecules and the radius are directly related to the energy magnitude of the interaction with the same scale factor to expand or contract them [28].

2.6.3. Docking simulation

Docking studies were carried out by Schrodinger-Maestro Version 10.7.014 [29] with extra precision (XP) docking module in Glide 5.5 (Grid-based ligand docking with energetics). Receptor structures of COX-1 (pdb ID: 1eqg) and COX-2 (pdb ID: 1pxx) have been downloaded from RCSB website (<http://www.rcsb.org/pdb/>) and subjected to receptors preparation including remove of crystallized ligands, water, cofactors as well as charge fixing and polar hydrogens were achieved. 2D ligands model were constructed via Maestro 2D sketcher application. The ligands **6a** and **6b** have been prepared by Ligprep application in Schrödinger that includes the minimization of energy, choosing proper chirality, addition of hydrogens, ring conformations and stereochemistry. The minimization has been achieved by OPLS (optimized potentials for liquid simulations) Model [30,31]. 3D Glide grid boxes have been generated with a size of (34x, 34y, 34z) Å³ and (32x, 32y, 32z) Å³ for COX-1 and COX-2 receptors, respectively with grid maps centred at 26.7, 33.9, 200.3 and 27.0, 24.1, 14.8 for COX-1 and COX-2, respectively. All the dockings have been performed for all receptor-ligand in Glide Extra Precision Mode active. The best ligand-receptor conformations are listed in Table 10, showing the glide score, docking score, glide energy, hydrogen bonds and Pi interactions. The visualization of results has been implemented by Maestro workspace, BIOVIA [32], LigPlot+ [33] and PyMol [34].

2.6.4. Molecular dynamic simulations

Molecular Dynamic stimulations (MDS) have been accomplished by using Desmond module (developed by D. E. shaw research) [35] embedded in Schrodinger-Maestro. The best conformation of the 6a-1eqg complex has been subjected to the molecular dynamics to investigate the stability of receptor-ligand complex system by immersing it in SPC (simple point charge) water model using orthorhombic box and OPLS 2005 force field. The system was neutralised by adding Cl⁻ ions. The neutralised system was built with 0.15 M concentration of salt (NaCl) in 10 Å buffer and the system was relaxed by implementing Steepest Descent and the limited-memory Broyden-Fletcher-Goldfarb-Shanno algorithms in a hybrid manner to ensure that there is no steric clashes or inappropriate geometry. The simulation was

Table 1
Crystal data and structure refinement details.

Parameter	Compound	
	6a	6b
CCDC Number	1842848	1828753
Empirical formula	C ₁₇ H ₁₁ ClF ₂ N ₂ O ₂ S	C ₁₈ H ₁₅ ClN ₂ O ₂ S
Formula weight	380.79	358.83
Temperature	293(2) K	293(2) K
Wavelength	0.71073 Å	0.71073 Å
θ range for data collection	2.326°–28.708°	2.305°–23.449°
Crystal system	Triclinic	Orthorhombic
Space group	<i>P</i> -1	<i>Pbca</i>
Cell dimensions	a = 8.9470(3) Å b = 10.0708(4) Å c = 10.5882(4) Å α = 76.763(3)° β = 88.242(2)° γ = 63.626(2)°	a = 17.2242(18) Å b = 9.6307(12) Å c = 20.581(2) Å α = 90° β = 90° γ = 90°
Volume	829.26(6) Å ³	3413.9(7) Å ³
Z	2	8
Density(calculated)	1.525 Mg m ⁻³	1.396 Mg m ⁻³
Absorption coefficient (μ)	0.391 mm ⁻¹	0.36 mm ⁻¹
F ₀₀₀	388	1488
Crystal size	0.15 × 0.20 × 0.25 mm	0.10 × 0.15 × 0.15 mm
Index ranges	-12 ≤ h ≤ 12 -13 ≤ k ≤ 13 -14 ≤ l ≤ 14	-19 ≤ h ≤ 19 -10 ≤ k ≤ 10 -23 ≤ l ≤ 23
Reflections collected	21870	35709
Independent reflections	4285	2502
Absorption correction	None	None
Refinement method	Full-matrix least-squares on F ²	Full-matrix least-squares on F ²
Data/restraints/parameters	4285/0/227	2502/0/219
Goodness-of-fit on F ²	1.016	1.039
Final R value [I > 2σ(I)]	R1 = 0.0439, WR2 = 0.1061	R1 = 0.0434, WR2 = 0.0824
R indices (all data)	R1 = 0.1096, WR2 = 0.1358	R1 = 0.0847, WR2 = 0.0993
Largest diff. peak and hole	0.217 and -0.265 e Å ⁻³	0.186 and -0.200 e Å ⁻³

Table 2
Selected Bond lengths(Å).

6a			6b		
Atoms	Length (Å)		Atoms	Length (Å)	
	Experiment	DFT B3LYP 6-311++G(d,p)		Experiment	DFT B3LYP 6-311++G(d,p)
S(2)–C(10)	1.712(3)	1.7368	S(2)–C(10)	1.707(3)	1.73714
S(2)–C(9)	1.719(2)	1.75214	S(2)–C(9)	1.722(3)	1.75187
O(15)–C(16)	1.365(3)	1.36468	O(15)–C(16)	1.387(3)	1.38442
O(13)–C(12)	1.221(3)	1.21757	O(13)–C(12)	1.222(3)	1.2177
N(11)–C(12)	1.352(3)	1.36558	N(11)–C(12)	1.352(4)	1.36814
N(11)–C(9)	1.385(3)	1.38779	N(11)–C(9)	1.389(4)	1.38749
C(21)–C(20)	1.366(4)	1.38462	C(21)–C(20)	1.364(4)	1.38738
C(20)–C(19)	1.357(5)	1.38337	C(20)–C(19)	1.387(4)	1.40278
C(4)–C(5)	1.396(3)	1.40269	C(4)–C(5)	1.388(4)	1.40263
C(17)–C(18)	1.364(4)	1.38481	C(17)–C(18)	1.387(4)	1.39834

Table 3
Selected Bond angles (°).

6a			6b		
Atoms	Angle		Atoms	Angle	
	Experiment	DFT B3LYP 6-311++G(d,p)		Experiment	DFT B3LYP 6-311++G(d,p)
C(10)–S(2)–C(9)	87.78(12)	87.6283	C(10)–S(2)–C(9)	87.86(15)	87.6233
C(16)–C(21)–C(20)	122.9(3)	122.4745	C(20)–C(21)–C(16)	120.4(3)	119.8504
F(22)–C(21)–C(16)	117.3(2)	117.8144	C(16)–C(21)–H(21)	119.8	118.8984
N(8)–C(7)–C(4)	119.7(2)	118.9470	N(8)–C(7)–C(4)	118.3(3)	118.9997
O(15)–C(14)–H(14B)	109.1	110.8969	O(15)–C(14)–H(14B)	108.5	106.0733
H(14A)–C(14)–H(14B)	107.8	108.7511	H(14A)–C(14)–H(14B)	107.5	107.9882
C(18)–C(17)–C(16)	122.2(3)	122.5198	C(16)–C(17)–C(18)	118.8(3)	119.2799
C(2)–C(1)–CL1	120.1(2)	119.6672	C(2)–C(1)–CL1	119.6(3)	119.6574
S(2)–C(10)–H(10)	124.1	119.6674	S(2)–C(10)–H(10)	124.0	119.6887
C(20)–C(19)–C(18)	121.5(3)	120.5929	C(18)–C(19)–C(20)	116.8(3)	117.5626

Table 4
Selected Torsion angles (°).

6a			6b		
Atoms	Angle		Atoms	Angle	
	Experiment	DFT B3LYP 6-311++G(d,p)		Experiment	DFT B3LYP 6-311++G(d,p)
C10–S2–C9–N8	0.2(2)	–0.0007	C10–S2–C9–N8	0.3(2)	0.0039
C10 S2 C9 N11	178.9(2)	–179.9898	C10 S2 C9 N11	179.3(3)	–179.6545
C9 S2 C10H10	179.5	–179.7011	C9 S2 C10H10	180	–179.1010
H11 N11C9 S2	178.7	–179.9480	H11 N11C9 S2	–177.6	179.9109
F22C21C20H20	–0.9	0.1615	H21C21C20H20	–0.1	0.1226
F22C21C20C19	179.0(3)	179.7731	H21C21C20C19	179.9	–179.5633
N8 C7 C10 S2	0.7(3)	–0.0653	N8 C7 C10 S2	–0.2(3)	–0.2294
O15C14C12 O13	176.4(2)	173.6256	O15C14C12 O13	–170.0(3)	–166.5139
F23C17C16 O15	–0.6(4)	–2.2192	O15C16C17H17	2	0.2333
C3 C2 C1 CL1	179.6(2)	179.9956	C3 C2 C1 CL1	–179.5(3)	–179.9891

Table 5
Hydrogen bond geometry (Å,°) of **6a** and **6b**.

6a					6b				
D–H ... A	D–H	H ... A	D ... A	D–H ... A	D–H ... A	D–H	H ... A	D ... A	D–H ... A
C(14)–H(14A) ... O(13) ⁱ	0.97	2.49	3.4176(1)	160	N(11)–H(11) ... O(13) ⁱ	0.86	2.24	3.0663(4)	162
C(19)–H(19) ... O(13) ⁱⁱ	0.93	2.52	3.4435(1)	169	C(5)–H(5) ... O(15) ⁱⁱ	0.93	2.59	3.2478(4)	128
Symmetry transformations: (i) –x,1–y,–z (ii) 1 + x,–1+y,z					Symmetry transformations: (i) 1/2–x,–1/2 + y,z (ii) –1/2 + x,1/2–y,–z (iii) 1/2–x,1/2 + y,z (iii) 1/2–x,1/2 + y,z				

Table 6
Selected charges accumulation and natural populations of **6a** and **6b** compounds.

Atom No.	Charge (e)	Natural population (e) of 6a			Total (e)	Charge (e)	Natural population (e) 6b			Total (e)
		Cor	Val	Ryd			Cor	Val	Ryd	
N8	–0.51939	1.99926	5.50101	0.01912	7.51939	–0.52126	1.99926	5.50289	0.01911	7.52126
S2	0.48039	9.99884	5.47642	0.04435	15.51961	0.48051	9.99884	5.47634	0.04430	15.51949
N11	–0.64177	1.99930	5.61682	0.02564	7.64177	–0.63438	1.99930	5.60912	0.02596	7.63438
H11	0.40436	0.00000	0.59139	0.00425	0.59564	0.40209	0.00000	0.59370	0.00421	0.59791
C12	0.67264	1.99945	3.28434	0.04356	5.32736	0.68183	1.99945	3.27537	0.04334	5.31817
O13	–0.58469	1.99976	6.57063	0.01429	8.58469	–0.59134	1.99976	6.57744	0.01414	8.59134
H14A	0.23686	0.00000	0.76074	0.00240	0.76314	0.19715	0.00000	0.80024	0.00261	0.80285
H14B	0.21343	0.00000	0.78473	0.00185	0.78657	0.21618	0.00000	0.78193	0.00189	0.78382
O15	–0.54525	1.99978	6.52807	0.01740	8.54525	–0.56553	1.99977	6.54928	0.01648	8.56553
F23	0.33808	1.99992	7.32749	0.01067	9.33808	^a 0.20586	0.00000	0.79141	0.00273	0.79414
C19	–0.18531	1.99921	4.16972	0.01637	6.18531	–0.02721	1.99907	4.01257	0.01556	6.02721
F22	0.33027	1.99992	7.32212	0.00823	9.33027	^b 0.21406	0.00000	0.78332	0.00262	0.78594
H19	0.21498	0.00000	0.78339	0.00164	0.78502	^c –0.57836	1.99927	4.57031	0.00878	6.57836

^a H17.^b H21 and.^c C22.

enhanced under NPT ensemble for 1.2 ns by implementing the Berendsen thermostat and barostat methods. With 300 K of temperature that maintained throughout the simulation using the Nose-Hoover thermostat algorithm [36] and 1.01325 bar of pressure through Martyna-Tobias-Klein Barostat algorithm [37]. The final production run was carried out for 1.2 ns and the trajectory sampling was done at an interval of 4.8 ps.

3. Results and discussions

3.1. Structural analysis

A block shaped colourless single crystals having dimensions 0.15 × 0.20 × 0.25 mm of **6a** and 0.10 × 0.15 × 0.15 mm for **6b** compound were chosen for Single crystal X-ray diffraction study, which revealed that the molecular systems were crystallized in different crystal systems, **6a** in the Triclinic with space group *P*-1,

and **6b** in the Orthorhombic system with space group *Pbca*. The details of structure refinement and descriptions of crystal data are given in Table 1. Fig. 1 illustrates the experimental ORTEP diagrams and predicted structure for the molecules. The dihedral angles between the planes of thiazole ring and ring **A** are 9.95° and 16.51° for **6a** and **6b**, respectively, indicating the coplanarity conformation. The noticeable change in conformation of the compounds based on the substituents can be observed between the mean planes of ring **A** with thiazole ring and ring **B** in **6a**, which indicated by mean planes angle values of 132.42°. The same angle has been shown in the **6b** with slightly smaller value of 83.58° (Fig. 2). The computed geometries of the compounds were compared with the experimental X-ray values. Some selected molecular parameters are listed in Tables 2–4 Full list of geometries are given in Tables S1–S3 of Supplementary Material. The atoms numbering is according to ORTEP diagram (Fig. 1).

In the present study, X-ray values of C–C bonds in rings **A** and **B**

Table 7
Selected Lewis and non-Lewis interactions from Second order perturbation theory analysis of Fock matrix for **6a** and **6b** molecules.

6a							6b						
Donor(i)	ED ^a	Acceptor(j)	ED ^a	E ⁽²⁾ kJ/mol	ΔE ^b	F(i,j) ^c	Donor(i)	ED ^a	Acceptor(j)	ED ^a	E ⁽²⁾ kJ/mol	ΔE ^b	F(i,j) ^c
π (C1–C2)	1.67848	π*(C4–C3)	0.35893	73.0108	0.30	0.065	σ(C1–CL1)	1.98927	σ*(C2–H2)	0.01274	34.47616	2.16	0.119
π(C3–C4)	1.62907	π*(C7–C10)	0.32303	65.85616	0.26	0.057	π(C3–C4)	1.62907	π*(C7–C10)	0.32332	64.05704	0.26	0.057
		π*(C5–C6)	0.31992	86.23224	0.27	0.067			π*(C5–C6)	0.31982	85.68832	0.27	0.067
		π*(C1–C2)	0.39375	94.64208	0.26	0.069			π*(C1–C2)	0.39410	94.39104	0.26	0.069
σ(C9–N11)	1.98241	σ*(N11–H11)	0.01469	379.2378	5.21	0.614	σ(C10–S2)	1.97306	σ*(C9–N11)	0.03689	21.63128	0.94	0.062
σ(C10–S2)	1.97303	σ*(C9–N11)	0.03704	21.7568	0.93	0.062			σ*(C4–C7)	0.03989	22.71912	1.03	0.067
		σ*(C4–C7)	0.03989	22.8028	1.03	0.067	σ(C2–C3)	1.97818	σ*(C4–C5)	0.02134	18.74432	1.06	0.062
σ(C9–N8)	1.98564	σ*(N11–H11)	0.01469	76.69272	5.36	0.280			σ*(C4–C7)	0.03989	15.85736	1.08	0.057
π(C9–N8)	1.87026	σ*(C19–H19)	0.01151	302.545	0.26	0.125			σ*(C3–C4)	0.02195	13.8072	1.24	0.057
		σ*(C17–F23)	0.02830	964.3702	0.04	0.087			σ*(C1–C2)	0.02780	13.93272	1.24	0.058
		σ*(C3–C2)	0.01574	824.4154	2.30	0.619	σ(C5–C6)	1.96779	σ*(C4–C7)	0.03989	16.19208	1.08	0.058
		σ*(C2–H2)	0.01273	336.017	2.45	0.408			σ*(C1–CL1)	0.03186	20.83632	0.83	0.057
		σ*(N11–H11)	0.01469	2034.972	4.35	1.338	σ(N11–H11)	1.96532	σ*(C9–S2)	0.07490	18.24224	0.84	0.055
σ(N11–H11)	1.96536	σ*(C12–O13)	0.01367	14.4348	1.16	0.057	π(C5–C6)	1.67877	π*(C3–C4)	0.35900	83.21976	0.29	0.068
		σ*(C9–S2)	0.07491	18.2004	0.84	0.054			π*(C1–C2)	0.39410	81.83904	0.27	0.066
σ(C12–N11)	1.98430	σ*(N11–H11)	0.01469	687.8496	5.15	0.822	σ(C7–N8)	1.97850	σ*(C9–N8)	0.03689	21.3384	1.10	0.067
σ(C12–O13)	1.99516	σ*(N11–H11)	0.01469	109.2861	5.57	0.341	σ(C9–S2)	1.97976	σ*(C10–H10)	0.01120	13.34696	1.13	0.054
π(C12–O13)	1.98633	σ*(N11–H11)	0.01469	793.9977	4.76	0.849	σ(C14–H14B)	1.96841	π*(C12–O13)	0.21121	23.97432	0.53	0.052
σ(C14–H14B)	1.96596	π*(C12–O13)	0.21087	24.81112	0.52	0.052	π(C16–C17)	1.67485	σ*(C18–C19)	0.33688	77.06928	0.30	0.067
π(C16–C17)	1.68511	π*(C19–C18)	0.34736	73.26184	0.31	0.066	σ(C17–H17)	1.97559	σ*(C16–C21)	0.02268	16.81968	1.09	0.059
σ(C21–F22)	1.99502	σ*(N11–H11)	0.01469	76.52536	5.57	0.286	π(C18–C19)	1.64995	π*(C16–C17)	0.39100	88.15688	0.26	0.067
π(C19–C18)	1.68325	π*(C16–C17)	0.43615	94.72576	0.24	0.068	π(C20–C21)	1.68077	π*(C18–C19)	0.33688	85.22808	0.29	0.069
π(C20–C21)	1.67075	π*(C19–C20)	0.34736	83.80552	0.29	0.068			π*(C16–C17)	0.39100	89.24472	0.27	0.069
		π*(C16–C17)	0.43615	87.27824	0.27	0.068	LP(1)N11	1.74837	π*(C12–O13)	0.21121	101.5457	0.34	0.082
LP(1)N11	1.75100	π*(C12–O13)	0.21087	102.6335	0.34	0.083			π*(C9–N8)	0.43144	73.55472	0.35	0.073
		π*(C9–N8)	0.43102	73.80576	0.34	0.073	LP(1)O15	1.96863	σ*(C16–C17)	0.02713	18.99536	1.15	0.064
LP(1)O15	1.97124	σ*(C16–C17)	0.03480	17.1544	1.12	0.060	LP(2)O13	1.85610	σ*(C12–N11)	0.08222	92.8848	0.59	0.104
LP(2)O13	1.85545	σ*(C12–N11)	0.08317	93.88896	0.59	0.104	LP(2)S2	1.59213	π*(C9–N8)	0.43144	126.9007	0.22	0.073
LP(2)S2	1.59196	π*(C9–N8)	0.43102	127.4446	0.22	0.073			π*(C7–C10)	0.32332	73.97312	0.26	0.062
		π*(C7–C10)	0.32303	73.55472	0.26	0.062							
LP(3)F22	1.92407	LP(3)F22	0.37501	76.7764	0.43	0.086							

^a Electron density.

^b Energy difference between donor orbital (i) and acceptor(j) orbital ΔE = E(i)–E(j) a.u.

^c F(i,j) is the Fock matrix element between i and j NBO orbitals in a.u unit.

Table 8
FMOs energy with global chemical parameters values of title compounds.

Property	Chemical parameters	6a	6b
LUMO energy	E _L (eV)	–1.841	–1.771
HOMO energy	E _H (eV)	–6.065	–6.0437
Energy gap	ΔE _{gap} = E _L – E _H (eV)	4.224	4.273
Ionization potential	I = –E _H	6.065	6.0437
Electron affinity	A = –E _L	1.841	1.771
hardness	η = (E _L – E _H)/2	2.112	2.1363
Softness	ζ = 1/2η	0.2367	0.2340
Chemical potential	μ = (E _L + E _H)/2	–3.953	–3.9073
Electronegativity	χ = –μ	3.953	3.9073
Electrophilicity	ψ = μ ² /2η	3.699	3.5732

from 1.357(5) Å to 1.396(3) Å, showing agreement with DFT predicted data (i.e., 1.38462 to 1.40278 Å) and also some reported thiazole compounds [38,39] have similar values. The small variations in the C–C bond lengths can be attributed due to the effects of the substituents present on different positions resulting with change in the charge distribution of the benzene ring [40,41]. This is clearly observed in the C–C bond lengths of rings **A** and **B** of the two molecules. In ring **A**, both the molecules are substituted by *p*-chloro showing no much deviation, while the different substituents and position in ring **B** reflected maximum difference of 0.01372 Å (0.021 Å) as mentioned by both DFT values and XRD in parenthesis. The substitution of methyl group (electron donating) at para position in ring **B** (**6b**) has shown an increase of the electrons density on the ring (see Table 6) resulting in the increase of length C19–C20 = 1.40278 Å (1.387(4) Å), which has the longest C–C bond lengths found in the phenyl ring **B**. On the other hand, the

substitution of two fluorine atoms (electron acceptor) at ortho positions in ring **B** (**6a**) has decreased the electron density at the ring carbon atom resulting in the reduction of lengths for C18–C17 = 1.38481 Å (1.364(4)Å), as well as C20–C19 = 1.38337 Å (1.357(5)Å), which has the shortest lengths of C–C bond as observed in the phenyl rings.

The effect of methyl group in ring **B** (**6b**) shows distortion in the ring yielding angles smaller than the typical angle (hexagonal) of 120°. at the position of substitution i.e. C18–C19–C20 = 117.5626° (116.8(3)°), recording the smallest C–C–C angle in the molecules [42]. This effect is in reverse with fluorine atoms (**6a**) that exhibited larger (120°). at the position of substitution i.e. C18–C17–C16 = 122.5198° (122.2(3)°) and C20–C21–C16 = 122.4745° (122.9°), respectively, recording the largest C–C–C angle for phenyl rings.

The variations in the bond length of phenyl rings **A** and **B** have been investigated by standard deviation equation (2):

$$\sigma = \sqrt{\frac{1}{N} \sum_{i=1}^N (x_i - \mu)^2} \quad (2)$$

where μ represent the mean.

The deviation in length of rings **A** and **B** for **6a** are (0.01048) Å and (0.00641) Å, respectively, showing the bond lengths of the ring **A** seems to be a double distorted than that of ring **B**.

While the deviation of rings **A** and **B** for **6b** are 0.00963 Å and 0.00955 Å, respectively, denoting that the distortions of bond lengths of the ring **A** and **B** are seem to be similar.

Over all standard deviation results indicated that the

Table 9

Different interaction energies (kJ/mol) of the molecules at B3LYP/6-31G(d,p). Symop: symmetry operation, R: Distance between molecular centroids (mean atomic position) in Å.

6a								6b							
N	Symop	R	E_ele	E_pol	E_dis	E_rep	E_tot	N	Symop	R	E_ele	E_pol	E_dis	E_rep	E_tot
2	x, y, z	10.07	-2.86	-0.444	-18.64	5.01	-16.49	2	x+1/2, -y+1/2, -z	9.02	-7.08	-0.814	-16.99	9.02	-15.86
1	-x, -y, -z	6.12	-10.10	-2.442	-70.81	29.29	-51.62	1	-x, -y, -z	5.90	-5.92	-1.48	-52.35	19.10	-40.65
2	x, y, z	16.2	-3.49	-0.444	-5.49	2.29	-6.69	2	x+1/2, -y+1/2, -z	11.41	-1.46	-0.15	-5.05	2.47	-4.19
1	-x, -y, -z	4.50	-14.16	-1.998	-64.28	22.5	-55.94	2	-x+1/2, y+1/2, z	5.94	-32.87	-4.59	-51.83	33.19	-56.10
1	-x, -y, -z	7.40	-10.89	-0.888	-30.57	13.41	-28.05	2	x, y, z	9.63	-4.65	-0.59	-8.19	4.57	-8.86
1	-x, -y, -z	9.12	-22.41	-3.404	-21.60	14.40	-29.61	2	-x+1/2, -y, z+1/2	11.16	-3.81	-0.52	-22.39	8.40	-18.32
2	x, y, z	10.07	-10.04	-1.406	-8.71	6.74	-12.01	2	x, -y+1/2, z+1/2	12.65	-1.90	-0.22	-5.84	2.35	-5.61
1	-x, -y, -z	11.21	-0.21	-0.592	-10.71	2.60	-8.32	2	x, -y+1/2, z+1/2	10.54	-1.90	-0.22	-13.07	5.44	-9.75
1	-x, -y, -z	15.14	-0.53	-0.074	-0.074	0.74	-4.58								
Total			-74.69	-11.692	-235.6	96.98	-213.31				-59.59	-8.584	-175.71	84.54	-159.34

Symop: symmetry operation, R: Distance between molecular centroids (mean atomic position) in Å

Table 10

Schrödinger Docking Results of 6a and 6b ligands with COX-1 and COX-2 protein receptors.

Ligands	Protein Receptor	Glide Score	Docking score	Glidevdw ^a	Glidecoul ^b	Glide energy kcal/mol	H bonds with Residues	H Bond length (Å)	Pi interactions	
									Pi-Pi	Pi-Cation
6a	1eqg	-8.919	-8.914	-39.85	-3.93	-43.79	TYR355:NH11 ARG120:O13	1.87 2.16	TYR355:Cg(2)	ARG120:Cg(3)
	1pxx	-6.834	-6.829	-13.91	-7.8	-21.67	TYR355:O13	1.7		ARG120:Cg(3) ARG120:Cg(1) ARG120:Cg(3)
6b	1eqg	-8.584	-8.579	-49.08	0.71	-48.37	ARG120:O13	1.93		ARG120:Cg(3)
	1pxx	-8.805	-8.800	-26.98	-1.31	-28.29	ARG120:O15	2.15	TYR355:Cg(3)	

^a Van der Waals and.

^b Coulomb interaction energies.

substituents of difluoro atoms at the ortho positions of ring **B** have more steric effect rather than the other ring **A**.

The agreement between the predicted values and experimental data were verified by using linear regression model with coefficient regression value of $R^2 = 0.99$ for both compounds, as shown in Fig. S9 of Supplementary Material. These results reflect the degree of agreement between theoretical and experimental data.

3.2. Supramolecular

H-bonds dominate in the supramolecular architecture of the crystal packing of **6a** molecule, where C19–H19...O13 interactions have linked the molecules into C9-chains when viewed down b-axis (Fig. 3I). The adjacent chains are interlinked via two centrosymmetric C14–H14A ... O13 bonds (Table 5), showing ring motif pattern $R^2_2(8)$, resulting in a chair type two-dimensional sheets in the ac plane (Fig. 3II). These sheets are stacked one over the other via weak interactions showing three-dimensional supramolecular feature (Fig. 3III).

On the other hand, the crystal packing of **6b** molecule down b-axis has showed C4-chain by connecting two molecules via N11–H11...O13 hydrogen bond with additional short contact

(O13...N11) (Fig. 4I). This chain is reinforced by weak C–H ... π interactions, showing C14–H14A ...Cg(3) = 2.74 Å and symmetry ($1/2-X, 1/2 + Y, Z$), where Cg(3) is the gravity centre of ring **B** (C16–C21). This C4-chain chain is constituted together with C6-chain via C14–H14B...N8 hydrogen bond. Altogether, these adjacent chains showed $R^2_2(8)$ ring motif. The neighbouring two motifs are linked by C10 chain via C5–H5...O15, S2...S2 short contacts as well as weak π ... π stacking, between Cg(1) thiazole ring and Cg(2) chlorophenyl ring, thereby forming into a two dimensional sheet when viewed along b axis (Fig. 4II). These sheets are further stabilized by C–H ... π interaction (with distance C20–H20 ... Cg(2) = 2.84 Å and symmetry operation ($1/2-X, -Y, 1/2 + Z$)), as seen in crystal packing (Fig. 4II). The geometries of potential hydrogen bonds are listed in Table 5.

3.3. First hyperpolarizability (β) and nonlinear optical property (NLO)

The First hyperpolarizability is a 3rd rank tensor described by 3D matrix ($3 \times 3 \times 3$) resulting in 27 components, and finally reduced to only 10 components [43], as computed by gaussian program according to formula (3) to get (β):

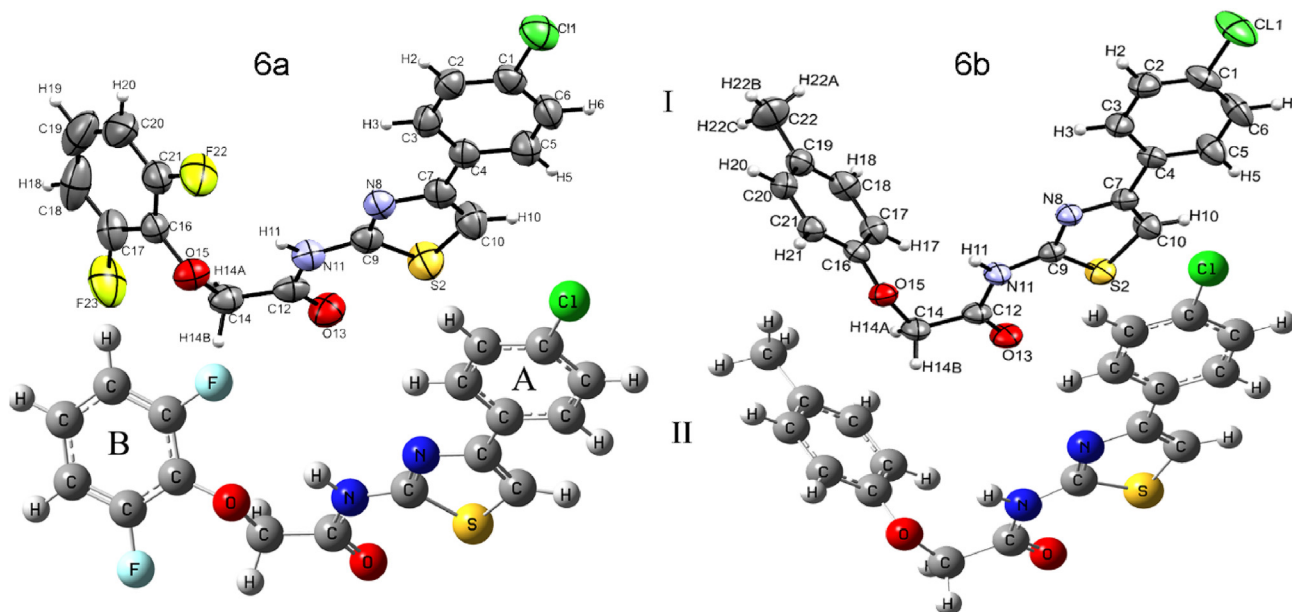


Fig. 1. Molecular structures of the molecules **6a** and **6b**: I) ORTEP diagrams drawn with 50% probability level and II) Optimized structures at DFT/B3LYP/6–311++G(d,p) level.

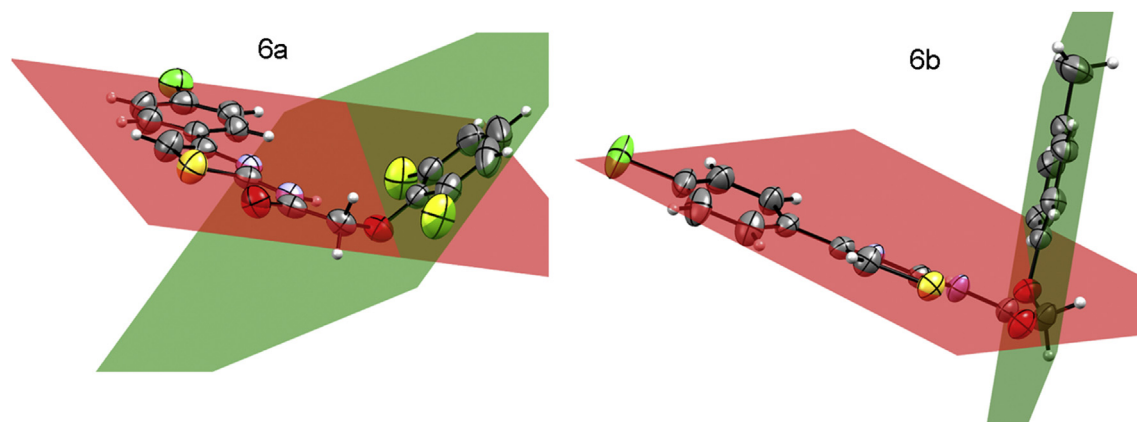


Fig. 2. **6a** showing with acute noncoplanar conformation (132.42°) and **6b** with perpendicular noncoplanar conformation (83.58°) between the designated mean planes (Shown in red colour and green colour).

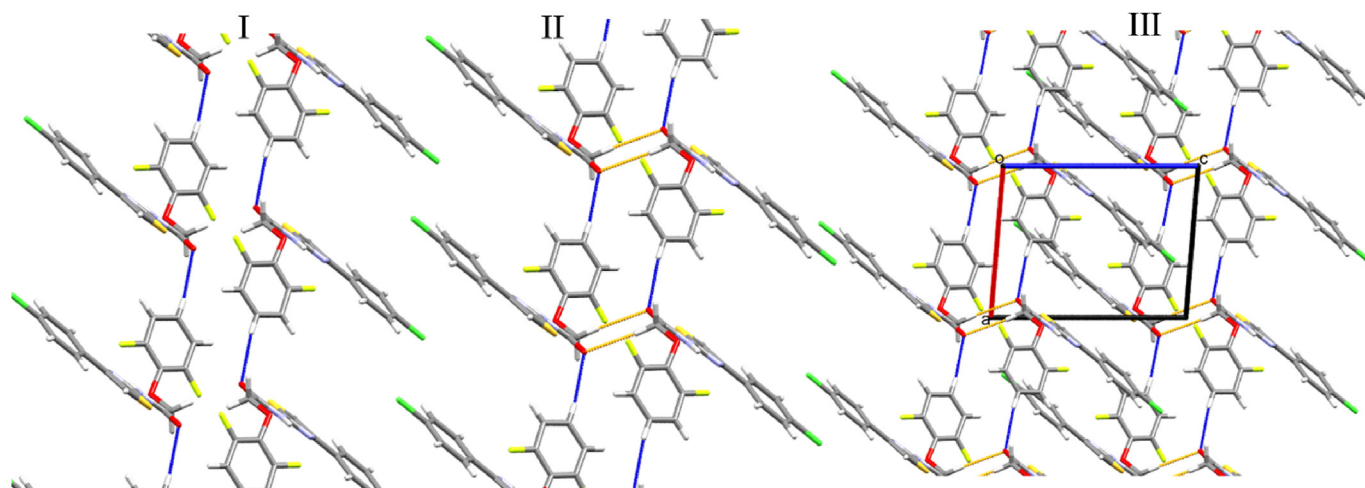


Fig. 3. Supramolecular architecture of the **6a** compound: I) one dimensional, II) two-dimensional chair-type sheets and III) three dimensional crystal packing viewed along b axis and showing two contacts C(19)–H(19) ... O(13) (blue) and C(14)–H(14A) ... O(13) (orange).

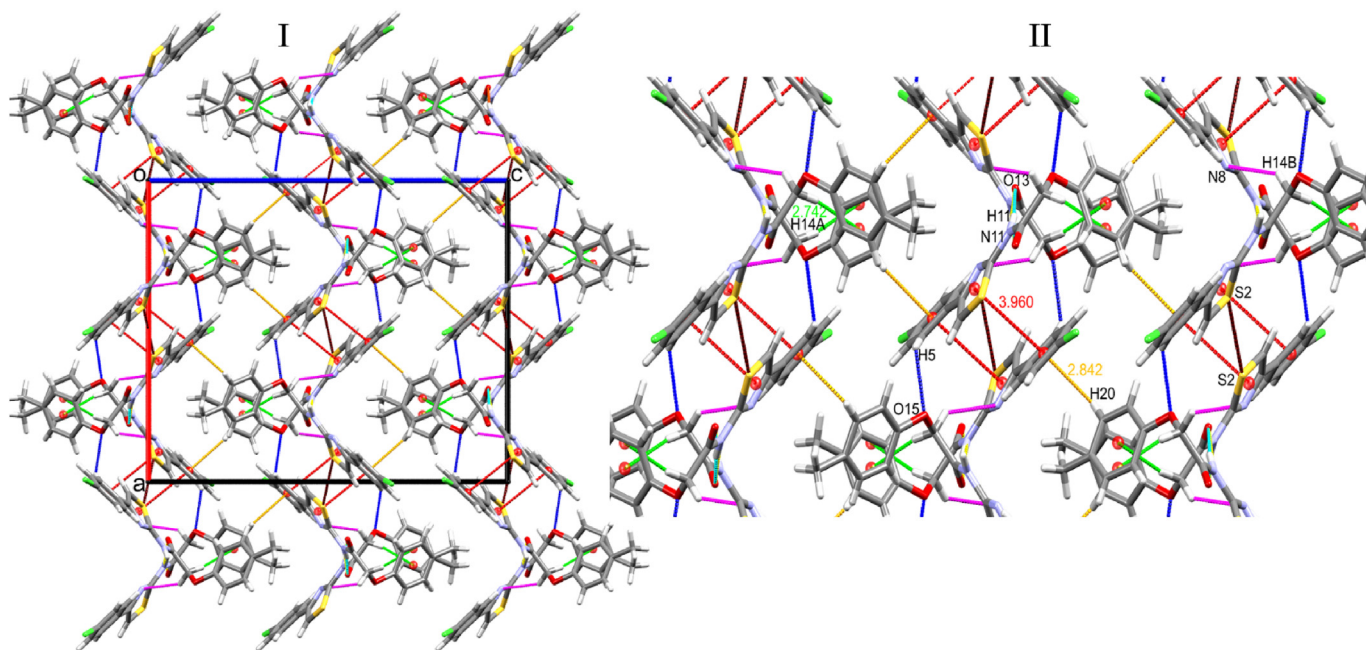


Fig. 4. Supramolecular architecture of **6b** compound: I) Crystal packing viewed down b axis. II) Close up view of crystal packing diagram showing diverse contacts: i) N11–H11...O13 (Turquoise), ii) C–H ... π : C14– H14B ...Cg(3) (light green), iii) C14–H14A ... N8 (magenta), iv) C5–H5...O15 (blue), v) S...S (brown), vi) π ... π : Cg(1) ... Cg(2) (red) and vii) C–H ... π : C20–H20 ...Cg(2) (black).

$$\beta = (\beta_x^2 + \beta_y^2 + \beta_z^2)^{1/2} \quad (3)$$

where, $(\beta_x^2 = \beta_{xxx}^2 + \beta_{xyy}^2 + \beta_{xzz}^2)$, $(\beta_y^2 = \beta_{yyy}^2 + \beta_{xxy}^2 + \beta_{yzz}^2)$ and $(\beta_z^2 = \beta_{zzz}^2 + \beta_{xxz}^2 + \beta_{yyz}^2)$

The computed β of **6a** and **6b** are 2.843×10^{-30} and 1.8671×10^{-30} respectively, in electrostatic units. In comparison with the KDP, β_{KDP} is 6.85×10^{-31} esu [44], but **6a** and **6b** are more than 4- and 2-times of KDP. The predicted dipole moment of former and latter are 4.2671 D and 3.6848 D respectively. The high values of computed β could be attributed to the non-zero dipole moment which indicates non-uniform distribution of the charges on the molecular atoms as well as the difference in molecular phase, due to theoretical isolated gas phase.

Experimentally, the nonlinear optical activity of both compounds is confirmed by using potassium dihydrogen phosphate (KDP) as reference material with $(I_2\omega: \text{KDP} = 17 \text{ mV})$. The results for **6a** and **6b** are 10 mV and 2 mV, respectively. These values give the SHG efficiency of **6a** and **6b** powdered samples of about 0.6 and 0.1 times of standard KDP. Accordingly, **6b** is just active for the NLO having very small value of SHG efficiency indicating that the para methyl group has less effect for NLO property, which may be due to non-coplanar conformation that exist between chlorophenyl ring and with other rings depicting almost perpendicular between them (see subsection 3.1) and also due to lack of the π -electron system (see subsection 3.4.2). In **6a**, the difluoro atoms in ortho position has shown enhanced NLO property with SHG efficiency exceeding the half value KDP standard material, and this could be ascribed due to the slightly acute noncoplanar conformation that exist between the rings (see subsection 3.1) showing abundance and redundancy of π -electron system. Hence, the degree of planarity influences the mobility of the electrons and also enhances NLO activity, while any deviations from planarity would decrease the mobility of electrons within the π -conjugated molecular system, resulting in the reduction of NLO activity [45,46].

3.4. Electronic structure

3.4.1. Natural population analysis (NPA)

The analysis of electron configuration on the natural atomic orbitals (NAOs) provide a satisfactory description of net natural atomic charge, with core (Cor), valence (Val), and Rydberg (Ryd) populations on each atom, which supports to understand the molecular properties [47]. The dissimilarities in energies and occupancies of **6a** and **6b** compounds are strongly proven the effects of the substitutions on the delocalization of charges that resulted in the variations of intermolecular contacts, angles and bond lengths (see section 2.2). The selected charge accumulations and electron configurations for all atoms in diverse sub-shells have been grouped in Table 6. Additional data of charges accumulation are presented in Table S4 of Supplementary Material.

For **6a** compounds, the highest electronegative charges of $-0.64177e$, $-0.58469e$, $-0.54525e$ and $-0.51939e$ are appearing on N11, O13, O15 and N8 atoms, respectively. However, in the case of **6b**, same atoms resemble the most of electronegative charges accumulation, but with slightly variation in magnitude of $-0.63438e$, $-0.59134e$, $-0.56553e$ and $-0.52126e$, respectively. The change in magnitude in this case can be attributed to the hydrogen bond formation from these atoms (see Table 5) as well as C22 atom of methyl group ($-0.57836e$). The maximum change in electronegativity of unsubstituted atoms C19 ($-0.18531e$) in **6a** and **6b** of C1 ($-0.02721e$) are observed, and this change can be attributed to hydrogen bond formation with **6a** (see Table 5). On the other hand, the most electropositive atoms in **6a** and **6b** are C12($0.67264e$, $0.68183e$), S2($0.48039e$, $0.48051e$) and H11($0.40436e$, $0.40209e$), respectively. The maximum change in electro positivity of hydrogen atoms are H14A ($0.23686e$) and H19($0.21498e$) in **6a**. These hydrogens are involved in hydrogen bonds for **6a** (see Table 5).

3.4.2. Natural bond orbital analysis (NBO)

The analysis of NBO provides the fairly information to portray

the delocalization effects between principal Lewis and non-Lewis orbitals, and further which shows the occupancy of electron loss from the filled Lewis orbital (donor) to the vacant non-Lewis orbital (acceptor). However, the significance and strengths of such interaction can be valued through the second order perturbation theory by applying the Fock matrix equation (4) [45–44].

$$E^{(2)} = \Delta E^{(2)}_{ij} = q_i F(i, j)^2 / \epsilon_j - \epsilon_i \quad (4)$$

where $E^{(2)}$, q_i is i th donor orbital occupancy, ϵ_i and ϵ_j are diagonal elements and $F(i, j)$ is the off-diagonal NBO Fock matrix (i is donor, j is acceptor). The magnitude of $E^{(2)}$ specify the strength degree of electron contributing from $i \rightarrow j$ orbitals, that demonstrates the intramolecular charge transfer (ICT) inside the molecular system [48]. The important selected results are tabulated in Table 7. More Lewis and non-Lewis interactions are given in Table S5 of Supplementary Material. The highest stabilization energy resulting from overlapping $\sigma \rightarrow \sigma^*$ in **6b** is formed between $\sigma(\text{C1-Cl1}) \rightarrow \sigma^*(\text{C2-H2})$ and $\sigma(\text{C10-S2}) \rightarrow [\sigma^*(\text{C4-C7}), \sigma^*(\text{C9-N11})]$ with $E^{(2)}$ values: 34.47616, 22.71912, 21.63128 kJ/mol, respectively. In **6a** the strongest $\sigma \rightarrow \sigma^*$ interactions resulted from overlapping between various bonds system $\sigma(\text{C12-N11}), \sigma(\text{C9-N11}), \sigma(\text{C12-O13}), \sigma(\text{C9-N8})$ and unique antibonding $\sigma^*(\text{N11-H11})$ with $E^{(2)}$ values of 687.8496, 379.2378, 109.2861, 76.69272 kJ/mol respectively. In both the molecules, the largest electron density (ED) value decreases for σ and increases in σ^* , that occurred via the interaction $\sigma(\text{N11-H11}) \rightarrow \sigma^*(\text{C9-S2})$, thereby indicate the importance of amide group in ICT and crystal packing (see subsection 3.2). The most significant $\pi \rightarrow \pi^*$ overlapping interactions in **6b** resulted from $\pi(\text{C3-C4}) \rightarrow \pi^*(\text{C1-C2})$ and $[\pi(\text{C20-C21}), \pi(\text{C18-C19})] \rightarrow \pi^*(\text{C16-C17})$ with $E^{(2)}$ of 94.39104, 89.24472, 88.15688 kJ/mol, respectively. While in **6a**, interactions resulted from $\pi(\text{C19-C18}) \rightarrow \pi^*(\text{C16-C17}), \pi(\text{C3-C4}) \rightarrow [\pi^*(\text{C1-C2}), \pi(\text{C20-C21})] \rightarrow \pi^*(\text{C16-C17})$ with $E^{(2)}$ of 94.72576, 94.64208, 87.27824 kJ/mol, respectively. The disparity of NBO of the compounds appear in the overlapping between the hybridization of π and σ orbitals, which are less significant in **6b** when compared to **6a**, thus such interaction in former compound reached maximum $E^{(2)}$ values of 77.06928, 23.97432 kJ/mol, owing to $\pi(\text{C16-C17}) \rightarrow \pi^*(\text{C18-C19})$ and $\sigma(\text{C14-H14B}) \rightarrow \pi^*(\text{C12-O13})$ respectively. But, hyper-conjugative interactions in **6a** resulted with the enormous stabilization energies with delocalization $E^{(2)}$ values of 2034.972,

964.3702, 824.4154, 793.9977 kJ/mol, which belong to $\pi(\text{C9-N8}) \rightarrow [\sigma^*(\text{N11-H11}), \sigma^*(\text{C17-F23}), \sigma^*(\text{C3-C2})]$ and $\pi(\text{C12-O13}) \rightarrow \sigma^*(\text{N11-H11})$, respectively. The ICT due to lone pairs in **6b** and **6a** are almost having similar association to the molecular stabilization values (Table 7).

3.4.3. Frontier molecular orbitals analysis (FMOs)

FMOs or HOMOs-LUMOs orbital indicate the highest occupied and lowest-unoccupied molecular orbitals, respectively [44]. The energy differences between these orbitals is named as energy gap (ΔE_{gap}), that provides very useful datum about the excited situation, electrical transport, chemical softness/hardness, chemical reactivity of molecular system [49]. The surfaces illustration of, ground state HOMO and first excited state LUMO are demonstrated in Fig. 5. The calculated energies of different FMOs, ΔE_{gap} and the values of global chemical parameters are summarised in Table 8.

The HOMO (ground state) orbitals are same for both compounds (Fig. 5), but with a few concentrations has been observed over the acetamide bridge (i.e., thiazole ring side chain) (Fig. 5). These electronic states are completely overturned in the first excited orbitals (LUMO) through **A** and **B** rings, where these can be understood as HOMO \rightarrow LUMO transition inferring the transfer of ED from chlorophenyl aromatic ring and acetamide bridge of the π -conjugated to the ring **B**, except CH₃ donor group (Fig. 5). Accordingly, the ΔE_{gap} and chemical reactivity parameters of the compounds are mainly connected to the thiazole ring and acetamide group reflecting their importance in electronic property and activity of molecules.

3.4.4. Electrostatic and molecular electrostatic potential (ESP & MEP)

The molecular electrostatic potential (MEP) is the 3D plot of electrostatic potential relating to the electron density mapped onto the iso-electron density surface.

Fig. 6I, delineates the ESP using the energy surface, where the negative electrostatic potential areas are convex bulge around (C11, N8, N11 and O13) atoms for both the compounds and as well as fluorine atoms for **6a** only. The zero potentials are designated by flat surface, as portrayed in chlorophenyl ring plane for the both compounds. Furthermore, the areas with electron lacking are displayed as completely concave surfaces curvature around methylphenoxy ring in **6b**, but for **6a** due to difluoro atoms it seems to be

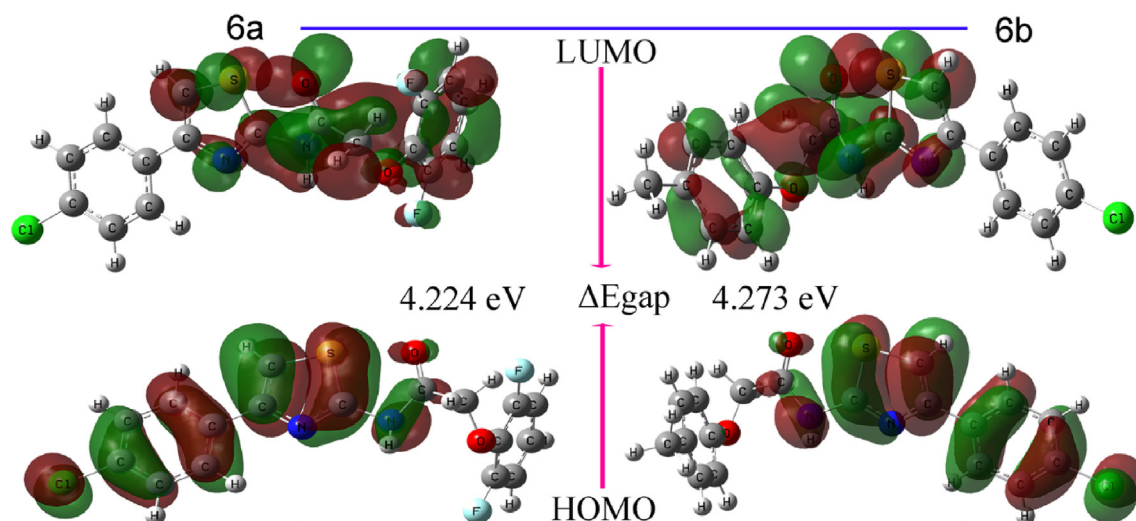


Fig. 5. HOMO-LUMO orbitals with energy gap.

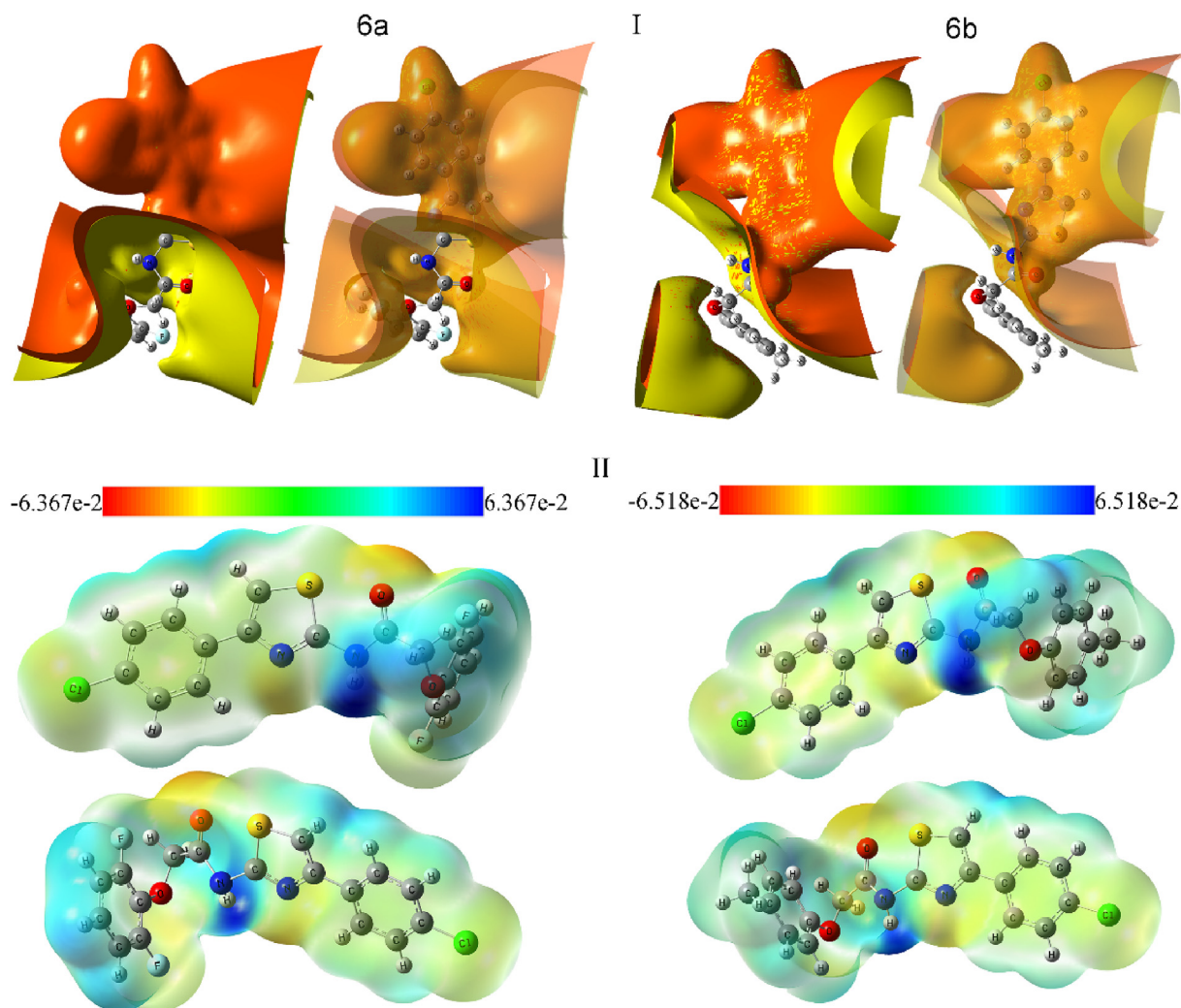


Fig. 6. I) ESP and II) MEP of **6a** and **6b** compounds obtained by DFT with B3LYP under 6–311++G(d,p) level.

relatively smaller electron deficient area, which confirms the more electronegativity nature of **6a** when compared to **6b**.

3D MEP is represented in the colour scheme that scaled from deepest red maximum electron concentration to deepest blue maximum electron deficient (Fig. 6II). The MEP of the both compounds are almost same with maximum electron concentration around O13, nucleophilic site, and maximum electron deficient about the (H11) atom, electrophilic site; this is justified by having N11–H11...O13 hydrogen bonds for both compounds) (see subsection 3.2). While the slightly less electron concentration represented by yellow colour is around O15, N8 and Cl1 atoms, respectively. But in addition to that, **6a** also exhibited light yellow colour around the fluorine atoms, which causes more electron deficient in para position of ring **B** (C19–H19) when compared to **6b**. As a result, the hydrogen bond: C19–H19...O13 is generated only for **6a** (see subsection 3.2). There are no much significant variations in zero potential regions, where light green colour is depicted on the chlorophenyl ring for both the compounds.

3.5. Hirshfeld surface

Hirshfeld surfaces of **6a** and **6b** have been constructed with volumes 419.14 Å³ and 419.14 Å³, respectively, (Fig. 7I). The colour

of d_{norm} is defined as -0.3861 au (blue) and 1.3711 (red) at distances longer and less than sum vdw radii, respectively. While white colour represents the exactly the sum of vdw radii with $d_{\text{norm}} = 0$. Both curvedness and shape index lie in the domain ranging from -4.00 to 4.00 and -1.00 to 1.00 respectively (Fig. 7 (II and III)) [50].

The different positions of bright-red spots on Hirshfeld surfaces shown for compounds in Fig. 7I, which proves the different substituents effect on the structure.

The Figs. of 2-D fingerprint allow us to identify the participation of all atoms to the Hirshfeld surfaces (Fig. 8a). Furthermore, the breakdown of entire contribution to atom pairs enable us to predict the significant contribution to the crystal packing formation (Fig. 8b-d).

The interactions O...H that appear as a pair of characteristic spikes in both **6a** and **6b** (Fig. 8b), have the highest contribution towards the packing of crystal, since: $d_i + d_e \approx 2.5$ Å and 2.25 Å, respectively. The short O...H bond in the latter refers to the presences of two donor atoms, namely, N and C atoms. These interactions are covered with 10.4% and 10.8% of Hirshfeld surface for **6a** and **6b**, respectively.

In **6b**, N...H interaction (Fig. 8c) is also contributing strongly toward the supramolecular architecture of crystal packing, where

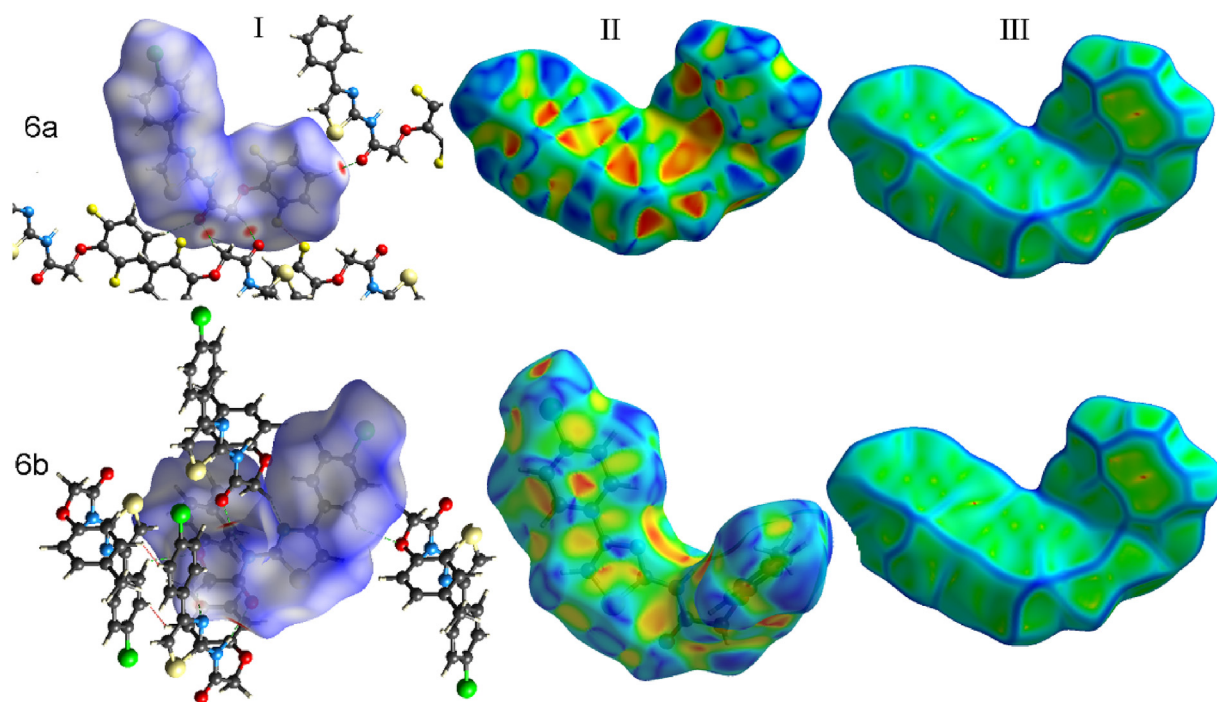


Fig. 7. Comparison of Hirshfeld surfaces for **6a** and **6b** molecules mapped over: (I) d_{norm} for representing the inter contacts and red spots denoting as hydrogen bonds, (II) Shape index and (III) Curvedness.

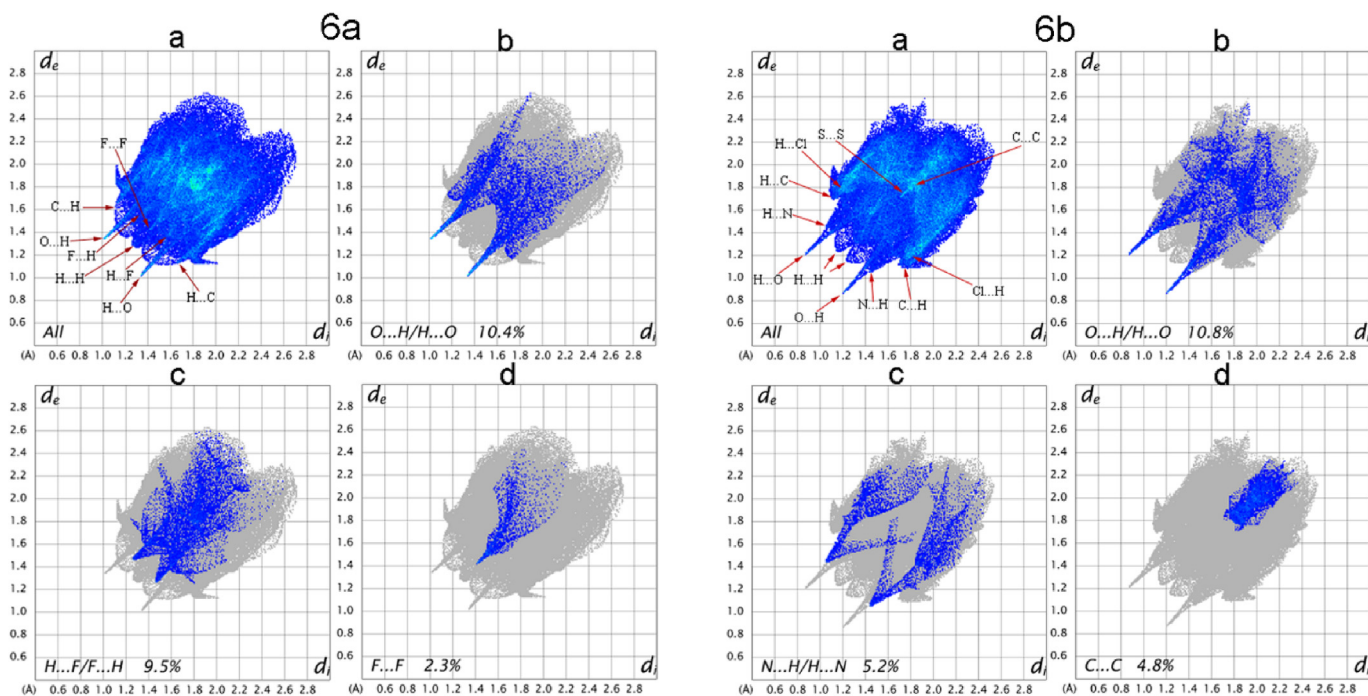


Fig. 8. 2D fingerprint plots of **6a** and **6b** showing: a) all contacts and (b–f) breakdown of contacts for specific pairs of atoms.

the atoms show contact distance at ≈ 2.60 Å, with 5.2% contribution to the Hirshfeld surface. The interatomic contacts $\text{F}\cdots\text{H}$ (Fig. 8c) and $\text{F}\cdots\text{F}$ (Fig. 8d) has 9.5% and 2.3% contribution to the Hirshfeld surface of **6a**, with insignificant contribution to the crystal packing is only from the latter, as short contacts with distance $d_i + d_e \approx 2.86$ Å $<$ 2.94 Å. For **6b**, the minor contribution from $\text{C}\cdots\text{C}$ contacts (4.8%) (Fig. 8d) also confirms the presence of $\pi \cdots \pi$

stacking in the crystal packing formation. This also could be shown on the shape index surface with pattern of blue and red triangles (Fig. 7b) as well as the flat regions upon the curvedness surface (Fig. 7c). The contribution of $\text{C}\cdots\text{H}$ and $\text{H}\cdots\text{H}$ to Hirshfeld surface for **6a** and **6b** comprising ranging from 34.3 to 19.1% with no directly contribution to the crystal packing as depicted in Fig. S10 of Supplementary Material.

3.6. Energy frameworks

The result analysis of energy frameworks for different types of interactions are listed in Table 9. The molecular environments of both **6a** and **6b** have been built by fixing one molecule in its centre and about with determined distance of 3.8 Å (Fig. 9). The benchmarked energies in this study have been scaled based on Mackenzie et al. [28]. While the scale factors for repulsion, polarization, electrostatic and dispersion interactions energies are 0.618, 0.871, 1.057 and 0.740, respectively [51]. In Fig. 9, the strengths of the energy framework are indicated by the cylinders. In general, the predicted interaction energies reveal the significance of the acetamide group in supramolecular architectures for both **6a** and **6b** as indicated in the energy framework (Fig. 9), showing with all strong cylinder energies in the region around it. The coulomb interactions in **6a** looks to be weaker in strength than in **6b** which could be justified by distance between molecular centroids (R) (see Table 9). This situation reverses for dispersion interaction (Fig. 9 (I)). However, in both molecules the dispersion interactions are predominant over electrostatics with values of energy reached $-235.6/-74.69$ kJ/mol and $-175.71/-59.59$ kJ/mol for **6a** and **6a**, respectively. The others including polarization and repulsion interaction energies are listed in Table 9, with total energies computed are -224.08 kJ/mol and 159.34 kJ/mol for **6a** and **6b**, respectively.

3.7. Docking simulation

The current *in silico* docking has been intended to check the inhibitor activity of **6a** and **6b** ligands against COX-1 and COX-2 protein receptors. Prior to docking simulations, the classical modes of inhibitor binding poses were observed experimentally in the COX active site, which contain inhibitors with Arg-120 of COX-1 and COX-2 [52], respectively. Instead, there could be also some apparent modes of NSAID binding that may result from differences in the speed and efficiency with which inhibitors can perturb the hydrogen bonding network around Arg-120 and Tyr-355 [53].

The results of Docking simulations revealed the prominent

interactions of **6a** and **6b** ligands with the active site residues of COX-1 and COX-2 (Fig. 10). The best glide score has been registered for **6a** ligand with COX-1 that binds at the active site with -8.92 kcal/mol and forms hydrogen bonds with ARG120:O13 and TYR355:O15 at distances of 2.16 and 1.87 Å, respectively. These bonds are similar to the co-crystal ligand bonding network and appears stronger (Fig. 11) [53]. Furthermore, there are pi-pi stacking interactions with TYR355 and Cg(2), as well as pi-cation interaction with ARG120 and Cg(3). In addition to latter, some hydrophobic interactions in the active site have been observed and found to be similar to the co-crystal ligand interactions as observed in COX1 (Fig. 12).

Fig. 13 represents three-dimensional surface plot mode showing the **6a** ligand enfoldment inside the active site cleft of COX-1 protein receptor with zoom view and ribbon model representations.

Table 10 lists the glide scores, hydrogen bonds, pi interactions and others parameters for all docking simulations that indicate the inhibitor activity of **6a** and **6b** compounds. We infer from the latter results that **6a** and **6b** are found to be potential COX-1 and COX-2 inhibitors, respectively, and these virtual results matches well with *in vitro* assay results (see Table 11). The other details of plots and conformation representations of all others docking simulations can be obtained from Supplementary Material (See Figs. S11–S15).

3.8. Molecular dynamics simulation

The results of MDS has ensured the stability of protein-Ligand complex (viz., **6a**-1eqg). The event trajectory was observed to remain stable throughout the simulation process. The stability of the system was tested by the root mean square deviation (RMSD) graph of the system during the simulation. Protein-ligand RMSD plot revealed that the system has been reached the stable form at 0.3 ns on the trajectory and later it loosed its stability after 1ns during the production run (Fig. 14A) Furthermore, the radius of gyration during the MDS was found to be within the range of 1 Å, indicating the compactness of the models predicted (Fig. 14A). This result has been supported by the Root Mean Square Fluctuation

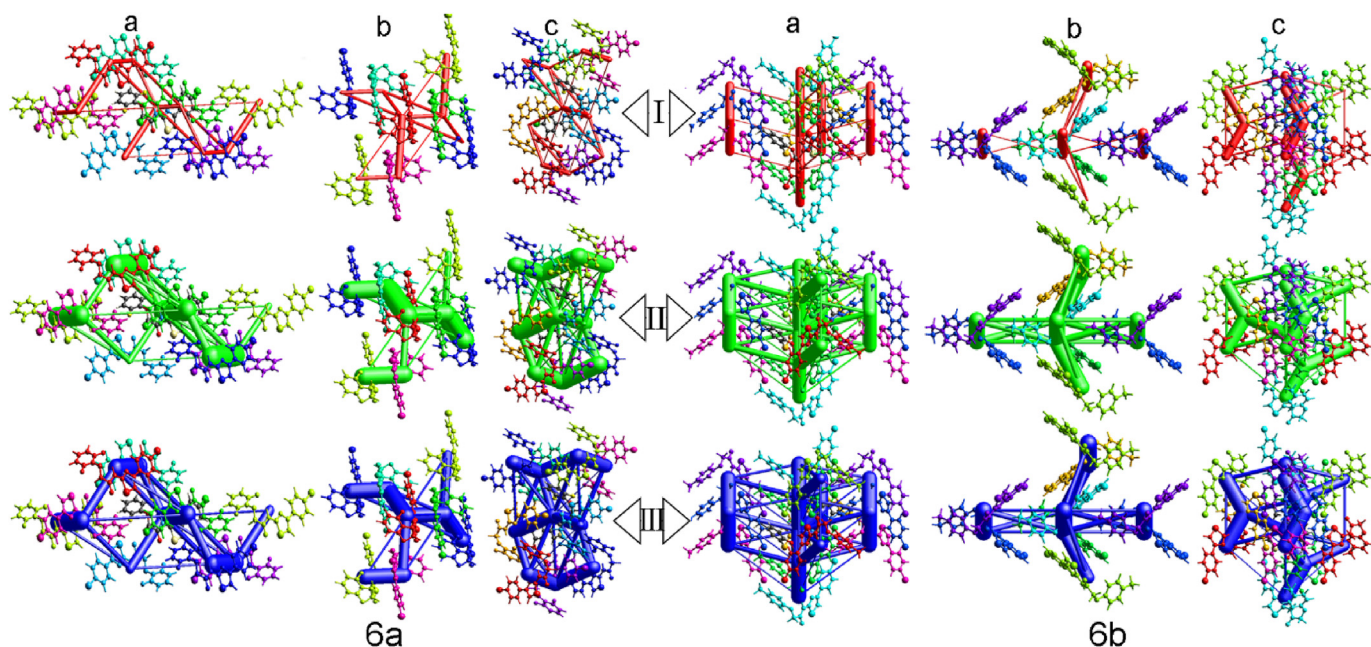


Fig. 9. Comparison of the interaction energies of **6a** and **6b** molecules: I) Coulomb interactions (red), II) Dispersion interactions (green) and III) Total interaction energies (blue) along a, b and c directions.

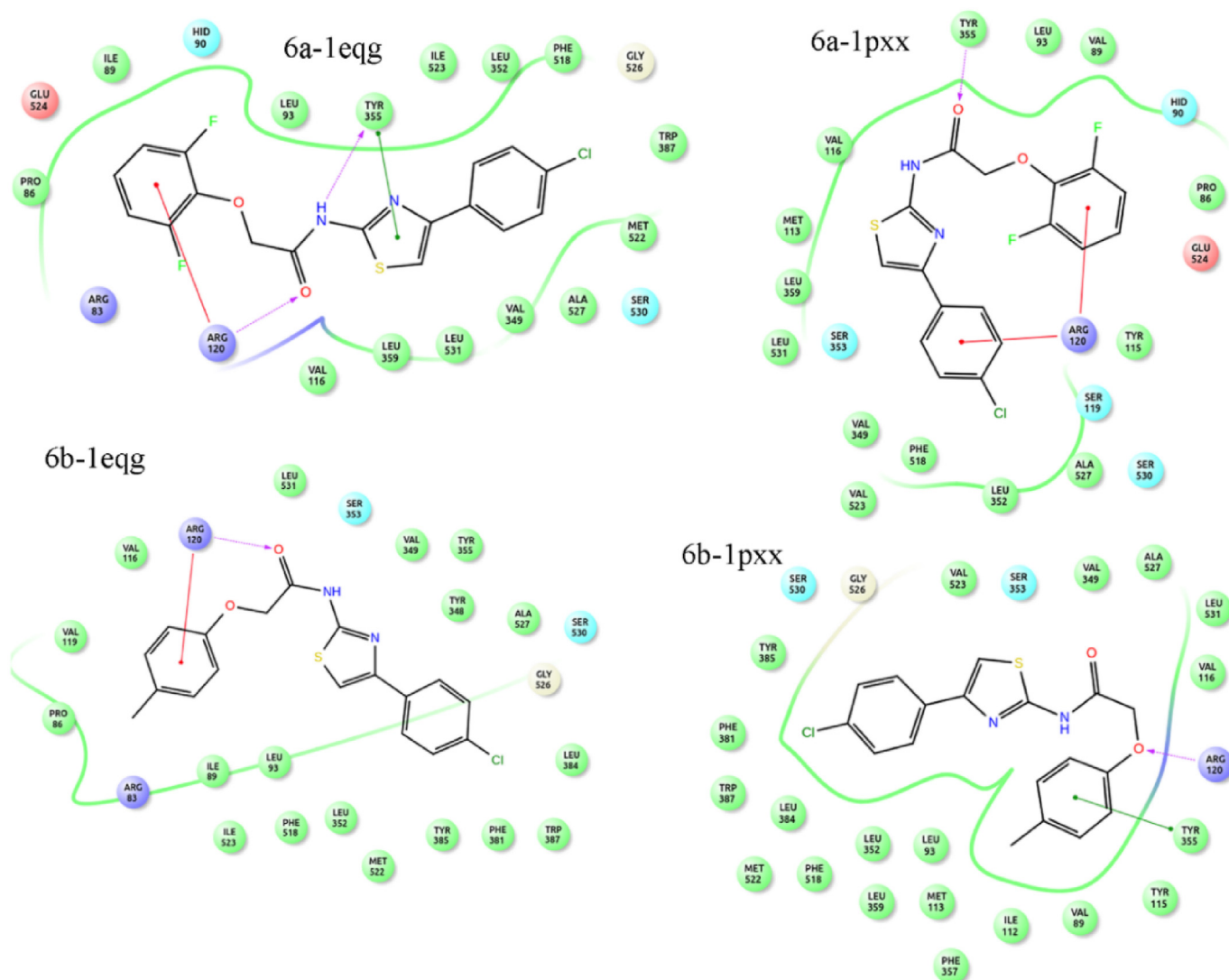


Fig. 10. Interaction plots of 6a and 6b ligands at the active site of protein receptors (pdb ID:1eqg and 1pxx).

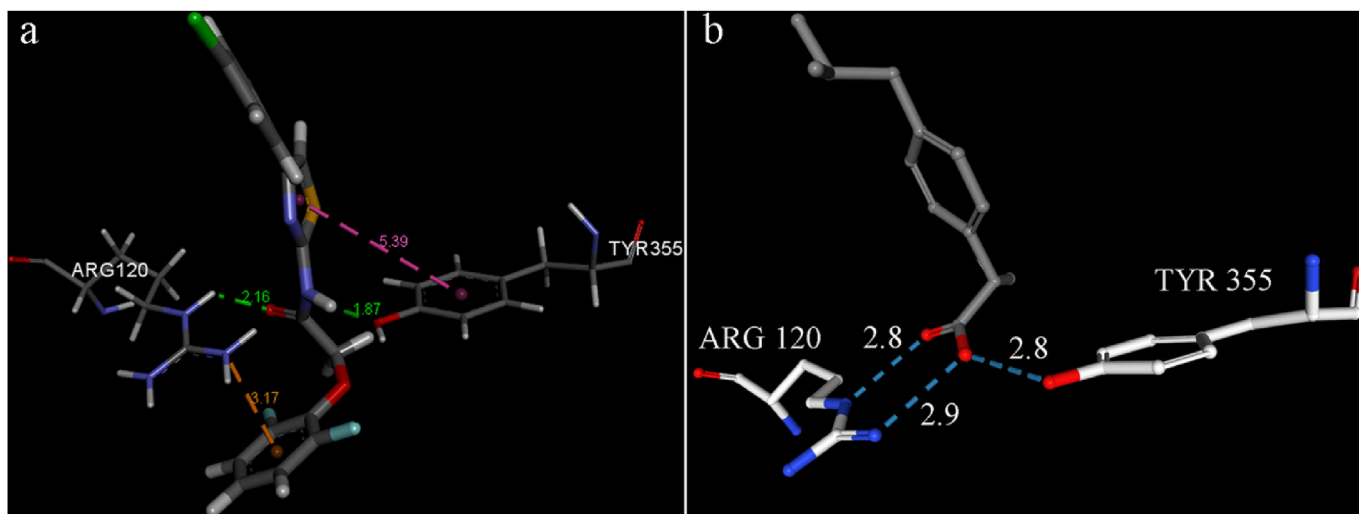


Fig. 11. Comparison of ligand interactions: a) 6a ligand and b) co-crystal ligand with 1eqg-COX-1.

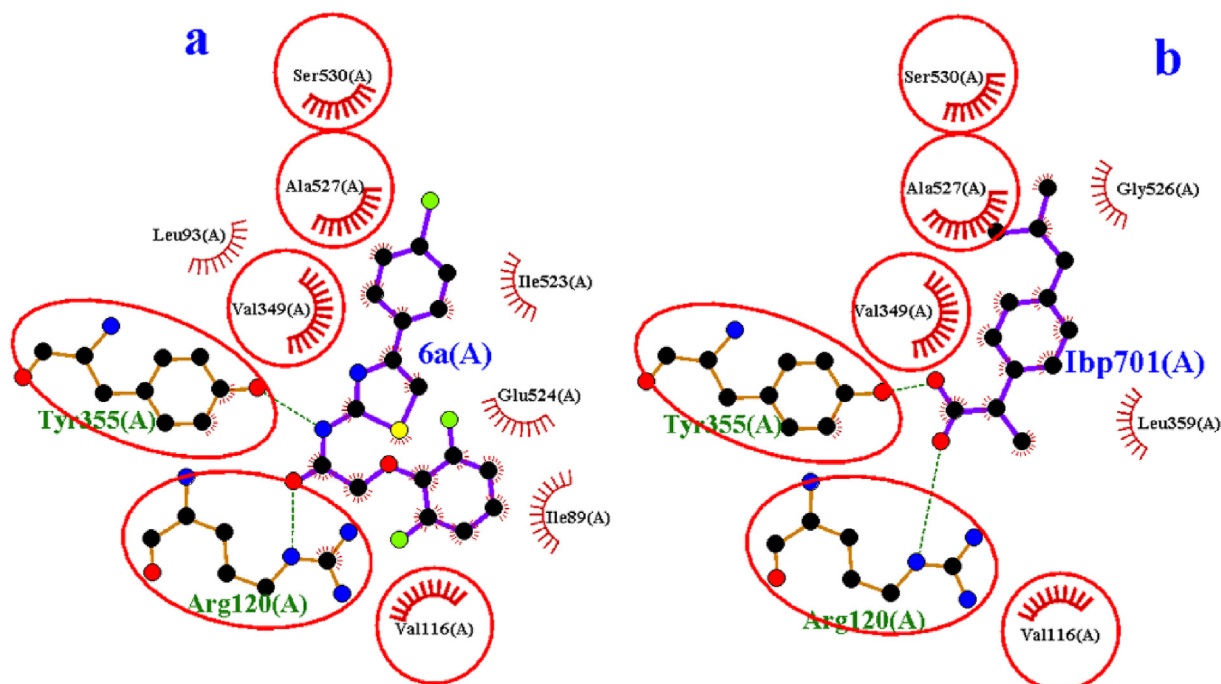


Fig. 12. Ligplot of hydrogen bond and hydrophobic interactions at the active site of 1eqg-COX1 protein receptor for: a) 6a ligand and b) co-crystal ligand.

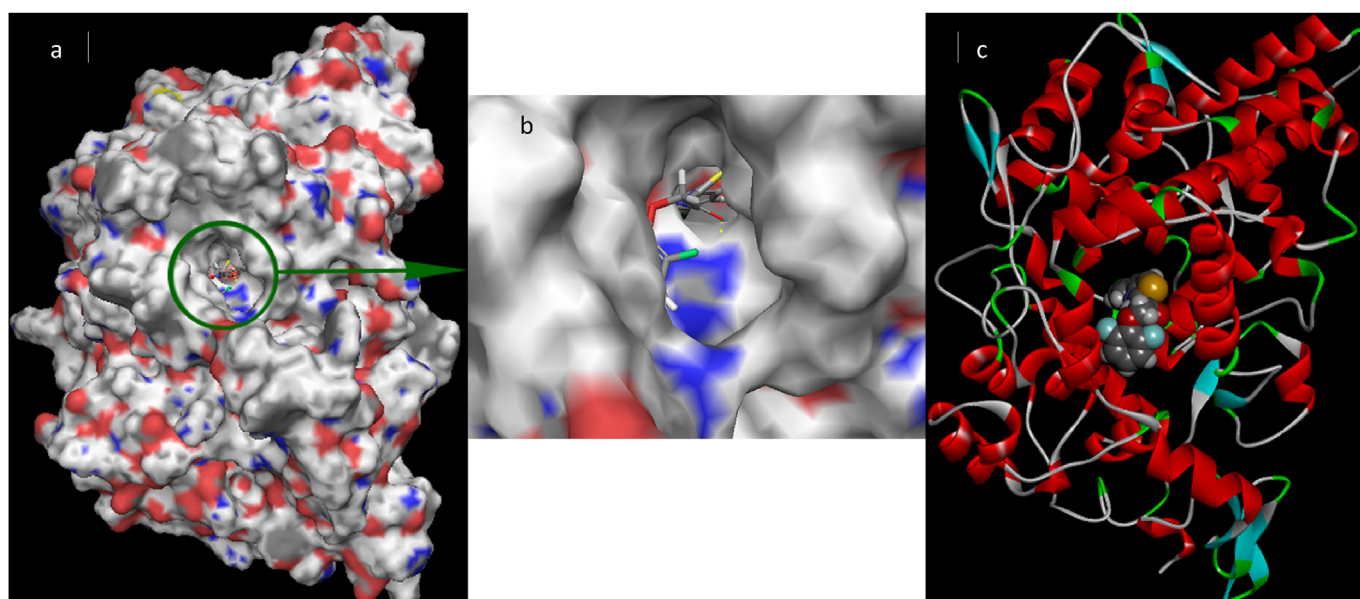


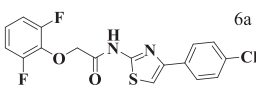
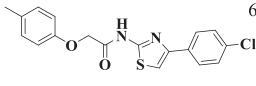
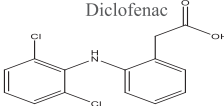
Fig. 13. a) 3D Surface view of 6a ligand, b) Zoom view of 3D surface showing active site groove region and c) Ribbon representation of protein receptor with CPK model of ligand.

(RMSF) plot (Fig. 14B) in which the residues fluctuations are found to be preferably more in the region where there is no much interactions involved with the ligands. Hence, these validation studies indicate the higher plausibility of the predicted models. On the other hand, the residues interactions with MDS results was also found to be almost similar with the docking results. The oxygen atom of carbonyl group displaying water bridged interaction with ARG120 has 82% presence, and also confirming the original hydrogen bonds with ARG120:O15 and TYR355:NH11, respectively. The pi-cation and pi-pi stacking interactions were also observed via thiazole ring towards ARG120 and TYR355, respectively (See Fig. 15).

3.9. Anti-inflammatory activity (cyclooxygenase (COX) inhibition)

One of the main biological activity of thiazole derivative is their ability to act as anti-inflammatory agent. A number of synthetic modifications, viz., with electron withdrawing/donating groups, heterocyclic infused, biphenyl based or other substitutions, have been reported to affect the anti-inflammation activities of thiazole derivatives [6,9–12]. The current study involves synthesis of heterocyclic compounds containing thiazole moiety and acetamide bridge (see Scheme 1). The efficacy of synthesized compounds **6a** and **6b** to inhibit ovine COX-1 and COX-2 enzymes was determined through measuring their peroxidase activity using colorimetric

Table 11
In vitro COX-1/COX-2 enzyme inhibition assay of the synthesized compounds with IC₅₀ (μM).

Compounds	IC ₅₀ (μM) ^a		COX-2SI ^b
	COX-1	COX-2	
 6a	10.21	9.11	1.12
 6b	18.2	3.13	5.81
 Diclofenac	7.9	8.2	0.96

^a IC₅₀ value is the compound concentration required to produce 50% inhibition of COX-1 or COX-2 for means of three determinations using an ovine COX-1/COX-2 assay kit. The deviation from the mean is <10% of the mean value.

^b Selectivity index (COX-1 IC₅₀/COX-2 IC₅₀).

enzyme immune assay. Then the inhibitory activity of synthesized compounds and standard compounds diclofenac were expressed with IC₅₀ values. The results of COX inhibition assay indicated that the tested compounds had a reasonable potent inhibitory activity against COX-2 with IC₅₀ = 9.11 μM & 3.1 μM respectively. Further, these compounds (**6a** and **6b**) exhibited COX-1 inhibition with IC₅₀ values of 10.2 μM & 18.2 μM, respectively, as listed in Table 11. The results of COX-1/COX-2 inhibition assay indicated that the compound **6b** showed excellent COX-2 inhibition. The *ortho*-difluoro

groups of **6a** also played a significant role in the COX-2 activity. IC₅₀ values of the compound **6b** with a para-methyl group has remarkably better COX-2 activity than COX-1. On overall, COX-2 activity for both the compounds show better inhibitory results.

4. Conclusion

Thiazole derivatives (**6a** and **6b**) have been synthesized and the final compounds were characterised via ¹H and ¹³C NMR as well as LC-MS mass spectra. Two single crystals were obtained and crystal structures were investigated by using X-ray diffraction method. Geometry parameters were calculated by using DFT method with B3LYP/6-311++G(d,p) basis set, and the results were in close agreement with the experimental parameters. NPA obtained by Second order Fock matrix analysis based on the charge accumulation revealed the reason behind for crystal packing environment with different hydrogen bonds. NBO also revealed the difference in stabilization and intramolecular charge transfer based on substituents. FMOs/ESP/MEP analyses showed the importance of the acetamide and thiazole moieties in the chemical reactivity descriptors of the molecules. The analysis of Hirshfeld surface with fingerprint plots revealed the types of interatomic contacts of molecules. Energy frameworks were examined based on the different intermolecular interaction energies. The activity of nonlinear optical property was determined by SHG experiment and substantiated by hyperpolarizability (β) parameter calculation and revealed the importance of fluorene atoms in the property. *In silico* molecular docking and dynamics simulations predicted potential COX inhibitor compounds 6a and 6b, showing the prominent interactions in the active sites of protein receptors. Further, summarizing the current investigations, we have efficiently synthesized some phenoxy thiazole acetamide derivatives **6a** and **6b** with fluoro

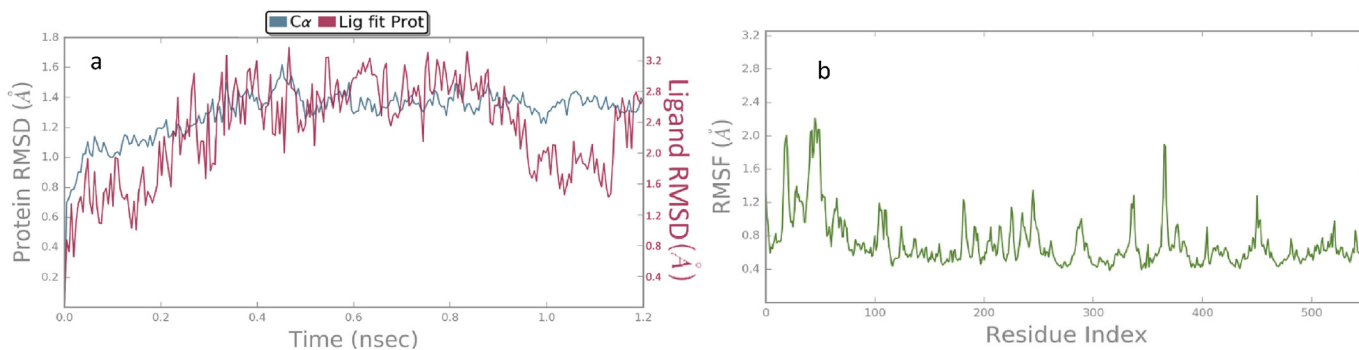


Fig. 14. a) RMSD and b) RMSDF plots of 6a-1eq complex.

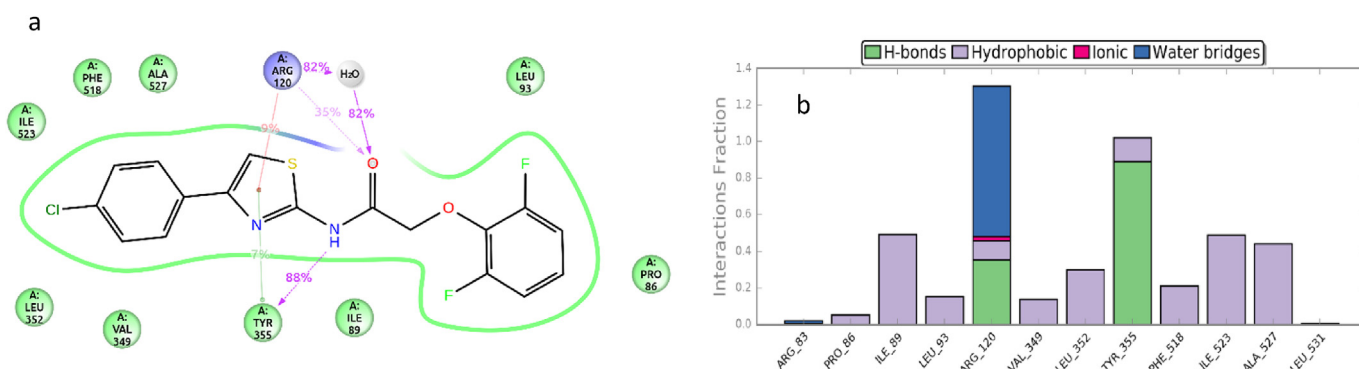


Fig. 15. a) 2D interaction poses and b) Histogram chart of the interaction percentages of the MDS for 6a-1eq complex.

and methyl groups at different position of benzoyl ring and also evaluated for anti-inflammatory activity. The activity data revealed that the compounds 6a and 6b showed better COX-1 and COX-2 inhibitory activity, respectively.

Acknowledgements

The authors would like to thank Dr. G. Hemantha Kumar, Coordinator of HPC, DOS in High Performance Computing and thankful to technical staff for providing Schrödinger application software and system in HPC Lab. And also, thanks to Mis. Lakshmi. R. S for assistance in MDS analysis. We are grateful to SAIF, IIT Madras, for providing single crystal and spectral data. Hussien Khamees wish to acknowledge the financial assistance provided by Abs Community College, Yemen. Yasser Hussein Eissa Mohammed is thankful to the University of Hajja, Yemen, for providing financial assistance. Fares Hezam Al-Ostoot gratefully acknowledges the financial support provided by government of Yemen and Albaydaa University-Yemen. Special thanks to Cytixon Bio solutions pvt. Ltd, Hubballi, India for biological assistance in this work. Shaukath Ara Khanum thankfully acknowledges the financial support provided by VGST, Bangalore, under CISEE Programme [Project sanction order: No. VGST/CISEE/282]. Dr. Mahendra M would like to thank University of Mysore for awarding research grant under the head DV6/375/MRP/2017–18, Dated:12-02-2018.

Appendix A. Supplementary data

Supplementary data to this article can be found online at <https://doi.org/10.1016/j.molstruc.2019.127024>.

References

- [1] M. T Chhabria, S. Patel, P. Modi, P. S Brahmshatriya, Thiazole: a review on chemistry, synthesis and therapeutic importance of its derivatives, *Curr. Top. Med. Chem.* 16 (26) (2016) 2841–2862.
- [2] H.A. Khamees, Y.H. Mohammed, A. Swamynayaka, F.H. Al-Ostoot, Y. Sert, S. Alghamdi, S.A. Khanum, M. Madegowda, Molecular structure, DFT, vibrational spectra with fluorescence effect, Hirshfeld surface, docking simulation and antioxidant activity of thiazole derivative, *Chemistry* 4 (15) (2019) 4544–4558.
- [3] Jaen, J. C., Wise, L., Teclé, D. H., & Bergmeier, S. C. (1987). (U.S. Patent and trademark office), U.S. Patent No. 3,896,223.
- [4] K. Z. Laczkowski, A. Biernasiuk, A. Baranowska-Laczkowska, K. Misiura, A. Malm, T. Plech, A. Paneth, Synthesis, antibacterial activity, interaction with nucleobase and molecular docking studies of 4-formylbenzoic acid based thiazoles, *Med. Chem.* 12 (6) (2016) 553–562.
- [5] Y. Lu, C.M. Li, Z. Wang, C.R. Ross, J. Chen, J.T. Dalton, L. Wei, D.D. Miller, Discovery of 4-substituted methoxybenzoyl-aryl-thiazole as Novel Anticancer Agents: synthesis, biological evaluation, and structure–activity relationships, *J. Med. Chem.* 52 (6) (2009) 1701–1711.
- [6] Ariyan, Z. S., & Kulka, W. A. (1975). (U.S. Patent and Trademark Office), U.S. Patent No. 3,896,223.
- [7] A.A. Geronikaki, A.A. Lagunin, D.I. Hadjipavlou-Litina, P.T. Eleftheriou, D.A. Filimonov, V.V. Poroikov, I. Alam, A.K. Saxena, Computer-aided discovery of anti-inflammatory thiazolidinones with dual cyclooxygenase/lipoxygenase inhibition, *J. Med. Chem.* 51 (6) (2008) 1601–1609.
- [8] M.N. Kumbhar, R.R. Kamble, J.P. Dasappa, P.K. Bayannavar, H.A. Khamees, M. Mahendra, S.D. Joshi, S. Dodamani, V.P. Rasal, S. Jalalpure, 5-(1-Aryl-3-(thiophen-2-yl)-1H-pyrazol-4-yl)-1H-tetrazoles: synthesis, structural characterization, Hirshfeld analysis, anti-inflammatory and anti-bacterial studies, *J. Mol. Struct.* 1160 (2018) 63–72.
- [9] P.K. Sharma, S.N. Sawhney, Potent antiinflammatory 3-thiazole-4 (5)-acetic acids of 1, 2-benzisothiazole, *Bioorg. Med. Chem. Lett* 7 (18) (1997) 2427–2430.
- [10] B.S. Holla, K.V. Malini, B.S. Rao, B.K. Sarojini, N.S. Kumari, Synthesis of some new 2, 4-disubstituted thiazoles as possible antibacterial and anti-inflammatory agents, *Eur. J. Med. Chem.* 38 (3) (2003) 313–318.
- [11] P.K. Deb, R. Kaur, B. Chandrasekaran, M. Bala, D. Gill, V.R. Kaki, R.R. Akkinipalli, R. Mailavaram, Synthesis, anti-inflammatory evaluation, and docking studies of some new thiazole derivatives, *Med. Chem. Res.* 23 (6) (2014) 2780–2792.
- [12] S.A. Rostom, I.M. El-Ashmawy, H.A.A. El Razik, M.H. Badr, H.M. Ashour, Design and synthesis of some thiazolyl and thiadiazolyl derivatives of antipyrine as potential non-acidic anti-inflammatory, analgesic and antimicrobial agents, *Bioorg. Med. Chem.* 17 (2) (2009) 882–895.
- [13] C.W. Dirk, H.E. Katz, M.L. Schilling, L.A. King, Use of thiazole rings to enhance molecular second-order nonlinear optical susceptibilities, *Chem. Mater.* 2 (6) (1990) 700–705.
- [14] E.M. Breitung, C.F. Shu, R.J. McMahon, Thiazole and thiophene analogues of donor–acceptor stilbenes: molecular hyperpolarizabilities and structure–property relationships, *J. Am. Chem. Soc.* 122 (6) (2000) 1154–1160.
- [15] S.H. Lee, A. Otomo, T. Nakahama, T. Yamada, T. Kamikado, S. Yokoyama, S. Mashiko, Novel rigid-rod 2, 6-diphenylbenzo [1, 2-d: 4, 5-d'] bisthiazole (DPBBT) derivatives for second-order nonlinear optical chromophores, *J. Mater. Chem.* 12 (8) (2002) 2187–2188.
- [16] H. Alyar, A review on nonlinear optical properties of donor-acceptor derivatives of naphthalene and azanaphthalene, *Rev. Adv. Mater. Sci.* 34 (2013) 79–87.
- [17] J. Zyss, I. Ledoux, S. Volkov, V. Chernyak, S. Mukamel, G.P. Bartholomew, G.C. Bazan, Through-space charge transfer and nonlinear optical properties of substituted paracyclophane, *J. Am. Chem. Soc.* 122 (48) (2000) 11956–11962.
- [18] K.D. Singer, J.E. Sohn, L.A. King, H.M. Gordon, H.E. Katz, C.W. Dirk, Second-order nonlinear-optical properties of donor-and acceptor-substituted aromatic compounds, *JOSA B* 6 (7) (1989) 1339–1350.
- [19] A. Leoni, A. Locatelli, R. Morigi, M. Rambaldi, Novel thiazole derivatives: a patent review (2008–2012. Part 2), *Expert Opin. Ther. Pat.* 24 (7) (2014) 759–777.
- [20] A.P.E.X. Bruker, SAINT-plus and SADABS, Bruker AXS Inc., Madison, Wisconsin, USA, 2004.
- [21] G.M. Sheldrick, Crystal structure refinement with SHELXL, *Acta Crystallogr. C* 71 (1) (2015) 3–8.
- [22] S.A. PLATON, An integrated tool for the analysis of the results of a single crystal structure determination, *Acta Crystallogr. A* 46 (1990) C34.
- [23] C.F. Macrae, I.J. Bruno, J.A. Chisholm, P.R. Edgington, P. McCabe, E. Pidcock, L. Rodriguez-Monge, R. Taylor, J.V. de Streek, P.A. Wood, Mercury CSD 2.0—new features for the visualization and investigation of crystal structures, *J. Appl. Crystallogr.* 41 (2) (2008) 466–470.
- [24] S.K. Kurtz, T.T. Perry, A powder technique for the evaluation of nonlinear optical materials, *Appl. Phys.* 39 (8) (1968) 3798–3813.
- [25] C. Lee, W. Yang, R.G. Parr, Development of the Colle-Salvetti correlation-energy formula into a functional of the electron density, *Phys. Rev. B* 37 (2) (1988) 785.
- [26] M.J. Frisch, et al., Gaussian 09, Gaussian Inc, Wallingford, 2009.
- [27] M.J. Turner, J.J. McKinnon, S.K. Wolff, D.J. Grimwood, P.R. Spackman, D. Jayatilaka, M.A. Spackman, CrystalExplorer. Version 17, University of Western Australia, 2017.
- [28] C.F. Mackenzie, P.R. Spackman, D. Jayatilaka, M.A. Spackman, CrystalExplorer model energies and energy frameworks: extension to metal coordination compounds, organic salts, solvates and open-shell systems, *IUCr* 4 (5) (2017) 575–587.
- [29] Maestro (Schrodinger LLC, 2009 (USA)).
- [30] W.L. Jorgensen, D.S. Maxwell, J. Tirado-Rives, Development and testing of the OPLS all-atom force field on conformational energetics and properties of organic liquids, *J. Am. Chem. Soc.* 118 (45) (1996) 11225–11236.
- [31] E. Harder, W. Damm, J. Maple, C. Wu, M. Reoubil, J.Y. Xiang, L. Wang, D. Lupyan, M.K. Dahlgren, J.L. Knight, J.W. Kaus, D.S. Cerutti, Goran Krilov, W.L. Jorgensen, OPLS3: a force field providing broad coverage of drug-like small molecules and proteins, *J. Chem. Theory Comput.* 12 (1) (2015) 281–296.
- [32] D.S. BIOVIA, Discover Studio Visualiser v19.10.18287, 2018 (San Diego, USA).
- [33] R.A. Laskowski, M.B. Swindells, LigPlot+: multiple ligand–protein interaction diagrams for drug discovery, *J. Chem. Inf. Model.* 51 (2011) 2778–2786.
- [34] The PyMOL Molecular Graphics System, Version 2.0 Schrödinger, LLC.
- [35] Desmond Molecular Dynamics System, Version 3.1, D.E. Shaw Research, New York, NY, 2012; Maestro-Desmond Interoperability Tools, version 3.1, Schrödinger, New York, NY, 2012.
- [36] D.J. Evans, B.L. Holian, The nose–hoover thermostat, *J. Chem. Phys.* 83 (8) (1985) 4069–4074.
- [37] G.J. Martyna, Remarks on “Constant-temperature molecular dynamics with momentum conservation”, *Phys. Rev. E* 50 (4) (1994) 3234.
- [38] F. Güntepe, H. Saraçoğlu, N. Çaliskan, Ç. Yüksektepe, A. Çukurovalı, Structure and DFT calculations of 2-[(3-methyl-3-phenyl-cyclobutyl)-thiazol-2-yl]-hydrazonomethyl-phenol, *J. Struct. Chem.* 52 (3) (2011) 596.
- [39] N. Çalişkan, F. Güntepe, Ç. Yüksektepe, A. Çukurovalı, O. Büyükgüngör, X-Ray diffraction and vibrational spectroscopic study of 2-chloro-N-{4-[3-(2, 5-dimethylphenyl)-3-methylcyclobutyl]-thiazol-2-yl}-acetamide, *Crystallogr. Rep. Crystallogr. Rep.* 55 (7) (2010) 1183–1187.
- [40] J.E. Boggs, F. Pang, P. Pulay, Structures of some fluorinated benzenes determined by ab initio computation, *J. Comput. Chem.* 3 (3) (1982) 344–353.
- [41] D.A. Dougherty, C.S. Choi, G. Kaupp, A.B. Buda, J.M. Rudziński, E. Ōsawa, Effects of substituents on the length of central C (sp³)–C (sp³) bond in anthracene photodimers and related molecules, *J. Chem. Soc. Perkin Trans. 1* (7) (1986) 1063–1070.
- [42] H.A. Khamees, M. Jyothi, S.A. Khanum, M. Madegowda, Synthesis, crystal structure, spectroscopic characterization, docking simulation and density functional studies of 1-(3, 4-dimethoxyphenyl)-3-(4-fluorophenyl)-propan-1-one, *J. Mol. Struct.* 1161 (2018) 199–217.
- [43] D.A. Kleinman, Nonlinear dielectric polarization in optical media, *Phys. Rev.* 126 (6) (1962) 1977.

- [44] G. Saravanakumar, G. Manobalaji, P. Murugakoothan, Experimental and theoretical investigations on N, N'-diphenylguanidinium dihydrogen phosphite—A semi-organic nonlinear optical material, *Spectrochim. Acta, Part A* 138 (2015) 340–347.
- [45] J.P. Abraham, D. Sajjan, V. Shettigar, S.M. Dharmaparakash, I. Némec, I.H. Joe, V.S. Jayakumar, Efficient π -electron conjugated push–pull nonlinear optical chromophore 1-(4-methoxyphenyl)-3-(3, 4-dimethoxyphenyl)-2-propen-1-one: a vibrational spectral study, *J. Mol. Struct.* 917 (1) (2009) 27–36.
- [46] G. Wipff, K. Morokuma, Nonplanarity of π systems. An ab initio study of norbornene and norbornadiene, *Tetrahedron Lett.* 21 (46) (1980) 4445–4448.
- [47] A.E. Reed, R.B. Weinstock, F. Weinhold, Natural population analysis, *J. Chem. Phys.* 83 (2) (1985) 735–746.
- [48] R.M. Jauhar, P. Era, V. Viswanathan, P. Vivek, G. Vinitha, D. Velmurugan, P. Murugakoothan, Crystal structure, molecular packing, FMO, NBO, nonlinear optical and optical limiting properties of an organic imidazolium diphenylacetate diphenylacetic acid single crystal, *New J. Chem.* 42 (4) (2018) 2439–2449.
- [49] F.A. Carey, R.J. Sundberg, *Advanced Organic Chemistry: Part A: Structure and Mechanisms*, second ed., Springer Science & Business Media, New York, 2007.
- [50] J.J. McKinnon, M.A. Spackman, A.S. Mitchell, Novel tools for visualizing and exploring intermolecular interactions in molecular crystals, *Acta Crystallogr. Sect. B Struct. Sci.* 60 (6) (2004) 627–668.
- [51] A.J. Edwards, C.F. Mackenzie, P.R. Spackman, D. Jayatilaka, M.A. Spackman, Intermolecular interactions in molecular crystals: what's in a name? *Faraday Discuss* 203 (2017) 93–112.
- [52] S.W. Rowlinson, J.R. Kiefer, J.J. Prusakiewicz, J.L. Pawlitz, K.R. Kozak, A.S. Kalgutkar, W.S. Stallings, R.G. Kurumbali, L.J. Marnett, A novel mechanism of cyclooxygenase-2 inhibition involving interactions with Ser-530 and Tyr-385, *J. Biol. Chem.* 278 (46) (2003) 45763–45769.
- [53] B.S. Selinsky, K. Gupta, C.T. Sharkey, P.J. Loll, Structural analysis of NSAID binding by prostaglandin H2 synthase: time-dependent and time-independent inhibitors elicit identical enzyme conformations, *Biochemistry* 40 (17) (2001) 5172–5180.